Diagnosis of 3D Vertical Circulation in the Upwelling and Frontal Zones East of Hainan Island, China

LINGLING XIE,[a,b] ENRIC PALLÀS-SANZ,[c] QUANAN ZHENG,[b] SHUWEN ZHANG,[a]
XIAOLONG ZONG,[d] XIAOFEI YI,[a] AND MINGMING LI[a]

[a] Guangdong Key Laboratory of Coastal Ocean Variability and Disaster Prediction, Guangdong Ocean University,
Zhanjiang, China
[b] Department of Atmospheric and Oceanic Science, University of Maryland, College Park, College Park, Maryland
[c] Departamento de Oceanografía Física, Centro de Investigación Científica y de Educación Superior de Ensenada,
Ensenada, Mexico
[d] Physical Oceanography Laboratory, Ocean University of China, Qingdao, China

ABSTRACT

Using the generalized omega equation and cruise observations in July 2012, this study analyzes the 3D vertical circulation in the upwelling region and frontal zone east of Hainan Island, China. The results show that there is a strong frontal zone in subsurface layer along the 100-m isobath, which is characterized by density gradient of $O(10^{-4})\,\text{kg m}^{-4}$ and vertical eddy diffusivity of $O(10^{-5}\text{–}10^{-4})\,\text{m}^2\,\text{s}^{-1}$. The kinematic deformation term S_{DEF}, ageostrophic advection term S_{ADV}, and vertical mixing forcing term S_{MIX} are calculated from the observations. Their distribution patterns are featured by banded structure, that is, alternating positive–negative alongshore bands distributed in the cross-shelf direction. Correspondingly, alternating upwelling and downwelling bands appear from the coast to the deep waters. The maximum downward velocity reaches $-5 \times 10^{-5}\,\text{m s}^{-1}$ within the frontal zone, accompanied by the maximum upward velocity of $7 \times 10^{-5}\,\text{m s}^{-1}$ on two sides. The dynamic diagnosis indicates that S_{ADV} contributes most to the coastal upwelling, while term S_{DEF}, which is dominated by the ageostrophic component S_{DEFa}, plays a dominant role in the frontal zone. The vertical mixing forcing term S_{MIX}, which includes the momentum and buoyancy flux terms S_{MOM} and S_{BUO}, is comparable to S_{DEF} and S_{ADV} in the upper ocean, but negligible below the thermocline. The effect of the vertical mixing on the vertical velocity is mainly concentrated at depths with relatively large eddy diffusivity and eddy diffusivity gradient in the frontal zone.

1. Introduction

The vertical circulation is one of the essential components of the ocean circulation system. In particular, in the coastal upwelling region and frontal zones, where high bioproductivity and active air–sea interactions occur, the vertical circulation serves as a carrier of vertical transport of mass and energy (Allen et al. 2005; Thomas et al. 2010; Ferrari 2011). Thus, determining the vertical circulation and its dominant mechanisms is an important work for understanding the physical and biogeochemical processes in the study ocean area (Pollard and Regier 1992; Barth et al. 2007; Nagai et al. 2008).

However, it is hard to measure the accurate vertical velocity directly using the state-of-the-art cruise observation

technologies. As a consequence, indirect methods have been developed to calculate the vertical velocity from the cruise data. The quasigeostrophic (QG) omega equation derived by Hoskins et al. (1978) has been broadly adopted for diagnosing the vertical circulation from the three-dimensional (3D) density fields in the frontal zones (Allen and Smeed 1996; Rudnick 1996; Shearman et al. 1999; Naveira Garabato et al. 2001; Hu et al. 2011). For motions with larger Rossby number, the generalized omega equation, a modified QG equation, has been developed by taking into account the ageostrophic advection and other non-QG terms (Viúdez et al. 1996; Giordani et al. 2006). Pallàs-Sanz and Viúdez (2005) used this equation for diagnosing the mesoscale vertical motion at the Atlantic jet and the western Alboran Gyre using conductivity–temperature–depth (CTD) and acoustic Doppler current profiler (ADCP) observations. They found that the non-QG terms are

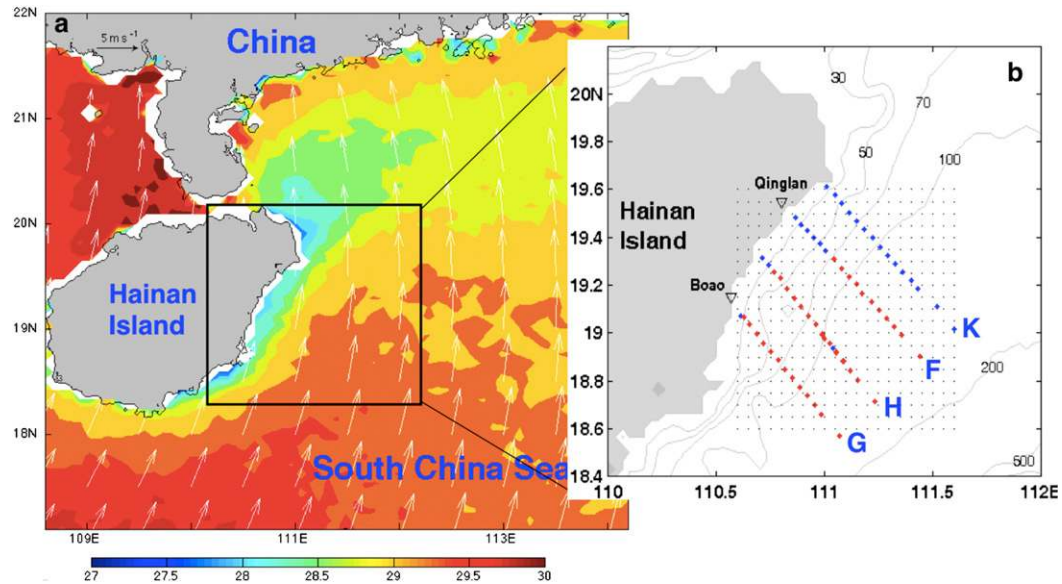Corresponding author e-mail: Lingling Xie, llingxie@umd.edu, llingxie@163.com

FIG. 1. (a) Map of the study area in the northern South China Sea. Background shows the climatological monthly SST (color, °C) and wind (white arrows) in July. (b) Map of cruise observation sections and stations. Red dots represent the stations with CTD, ADCP, and TurboMAP measurements. Blue dots are stations without TurboMAP measurements. Black dots are interpolation grids. Gray lines are isobaths (m). Qinglan and Boao are two landmarks at the coast.

important for calculation of the vertical circulation in the case of the large Rossby number. Pallàs-Sanz et al. (2010b) further modified the generalized omega equation by including the effects of the vertical mixing and found that the vertical velocity is quite sensitive to the vertical mixing parameterization.

This study is interested in the vertical circulation in a coastal upwelling region accompanied with strong ocean fronts on the continental shelf east of Hainan Island of China, as shown in Fig. 1a (Xie et al. 2012; Jing et al. 2015). Previous investigators have estimated the upwelling velocity based on conservation of the salinity flux and fluctuation of the isopycnals from hydrographic observations (Han et al. 1990; Wu 1990; Deng et al. 1995) and by numerical models driven by wind (Guo and Shi 1998; Su and Pohlmann 2009). Their estimated vertical velocities vary within a range of two orders of magnitude from 5.6×10^{-6} to $2 \times 10^{-4} \, \mathrm{m \, s^{-1}}$, implying that there is a big uncertainty in the estimated values of this key parameter for coastal ocean dynamics. Meanwhile, there is little knowledge about the 3D structure of the vertical circulation in the coastal upwelling and associated frontal zones. The effects of the vertical mixing on the vertical circulation also need to be clarified with the directly measured microstructure data. These challenges motivate us to apply the generalized omega equation to diagnose the vertical circulation in the study area, using in situ data of CTD, ADCP, and the microstructure mixing cruise observed in July 2012. This paper is

organized as follows: The next section describes the cruise observation program, the data processing, and the generalized omega equation. Section 3 examines the observed 3D density, horizontal velocity, and mixing fields. Section 4 diagnoses the dynamic terms in the generalized omega equation. Section 5 analyzes the 3D structure of the vertical circulation and contributions of each dynamic term. Sections 6 and 7 give discussion and conclusions.

2. Data and methodology

a. Cruise observation program

A joint physical and biogeochemical measurement program was carried out by R/V *Tianlong* of Guangdong Ocean University on the northwestern continental shelf of the South China Sea (SCS) in July 2012. As shown in Fig. 1b, cruise observations were conducted along four cross-shelf sections G, H, F, and K in the continental shelf water east of Hainan Island from 13 to 18 July 2012. The cross-shelf sections are spaced by about 25 km, and the stations are spaced by about 5 km. The observed depths are down to 150 m. The dataset includes CTD profiles with SBE 19 plus manufactured by Seabird Inc., horizontal velocity measurements with a 300k Hz ADCP manufactured by RD Instruments Inc., and microstructure mixing measured by TurboMAP-L of JFE Advantech. With the pre/postcruise calibration, the accuracy of the CTD sensors is about $0.0005 \, \mathrm{S \, m^{-1}}$ for the conductivity, $0.005°C$

for the temperature, and 1 dbar for the pressure. The bin size of ADCP measurements was set to 4 m, and the sampling time interval was set to 30 s. The ADCP was hung at about 6 m below the ocean surface on the windward side of the R/V when it stopped and thus allowed continuous observations for 5 min at the shallowest station and 50 min at the deepest station. The accuracy of the velocity is $2.0 \, \text{cm} \, \text{s}^{-1}$. The maximum range of TurboMAP-L equipped with two shear sensors (airfoil) is 500 m with a sampling rate of 512 Hz. At each station, TurboMAP-L was deployed 2–3 times to obtain repeated profiles. The observed high-frequency shear fluctuation data are used to estimate the dissipation rate of the turbulent kinetic energy. Noise level of the turbulent dissipation rate is less than $1 \times 10^{-10} \, \text{W} \, \text{kg}^{-1}$.

b. Data processing and interpolation

The raw CTD data are quality controlled and averaged into 1-m bins. The profiles are then smoothed by a 3-m boxcar moving average. Then density profiles and squared Brunt–Väisälä frequency N^2 with a 1-m resolution are calculated. ADCP measurements provide east u and north v current components with a vertical resolution of 4 m. The u/v profiles at each station are averaged over time of about 5–50 min depending on the depth. Thus, the high-frequency variation variations are eliminated from the time-averaged velocity profile.

From microstructure shear measurements by airfoil probes, the 2-m turbulent kinetic energy dissipation rate ε can be estimated (Zhang et al. 2012). Most ε profiles have reliable values at depths below 7 m, where the profiler is in a required quasi-freefall state and the shear spectra from observations for estimating ε compare well with the Nasmyth universal spectrum. The averaged ε profiles from repeated observations at each station are used to calculate the turbulent eddy diffusivity K_v using the formula $K_v = 0.2\varepsilon/N^2$ (Osborn 1980).

To obtain a regular gridded 3D matrix for vertical velocity calculation, the density, ADCP horizontal velocity components, and the eddy diffusivity are horizontally interpolated with linear interpolation. The grid sizes in the x and y directions are both set to be 0.05°. The interpolation ranges are 18.6°–19.6°N and 110.6°–111.6°E, as shown in Fig. 1b. The gridded data are then smoothed with a 2D Gaussian filter with scales of $Lx = 35 \, \text{km}$ and $Ly = 25 \, \text{km}$. These values are chosen to minimize the singularity generated in differential calculation and filter out contamination of small-scale processes but not to damage the essential spatial patterns. The vertical grid is set to be 5 m, and the depth range is 0–160 m. The density, velocity, and eddy diffusivity profiles from observations are averaged in the depth bins of 0, 5, 10, . . . , 160 m. For bins without observations near the surface and bins close

to but above the ocean bottom, values are extrapolated using the nearest observed data. Specifically, the density profiles are extended to the surface with constant values as that in the observed first bin in the mixed layer and to the bottom with linear extrapolation to keep the stratification. The velocities near the surface are filled with the topmost observations at about 10 m, while the velocities below the last observed bins are assumed to decrease linearly to zero at the ocean bottom (no-slip boundary condition). The eddy diffusivities near the surface are reasonably filled with the topmost values from observations at stations where the mixed layer is deeper than the first observation depth and assumed to be 10 times larger if the mixed layer is shallower than the first observation depth. Thus, we obtain the 3D gridded dataset, which has $(nx, \, ny, \, nz) = (21, 21, 33)$ nodes with grid sizes $(\Delta x, \, \Delta y, \, \Delta z) = (5 \, \text{km}, 5 \, \text{km}, 5 \, \text{m})$.

c. Calculation of geostrophic and ageostrophic velocities

Using the gridded 3D density data, the geostrophic velocities referred to a no motion depth are derived from the thermal wind balance:

$$u^g(x_i, y_j, z_k) = u_{\text{ref}}(x_i, y_j) + \int_{z_{\text{ref}}}^{z_k} \frac{\partial u}{\partial z} \, dz = 0 + \int_{z_{\text{ref}}}^{z_k} \frac{1}{f} \frac{\partial \varrho}{\partial y} \, dz, \tag{1}$$

and

$$v^g(x_i, y_j, z_k) = v_{\text{ref}}(x_i, y_j) + \int_{z_{\text{ref}}}^{z_k} \frac{\partial v}{\partial z} \, dz$$
$$= 0 + \int_{z_{\text{ref}}}^{z_k} -\frac{1}{f} \frac{\partial \varrho}{\partial x} \, dz. \tag{2}$$

Here, u^g and v^g are the east and north components of geostrophic velocity at depth bin z_k and station grid x_i, y_j, u_{ref} and v_{ref} are the velocity components at the reference depth, $f = 2\Omega \sin\varphi_0$ is the Coriolis parameter at the mean latitude φ_0, and $\varrho = -b = \rho_0^{-1} \rho g$ is the negative buoyancy b with ρ_0 as the mean density and g as the gravitational acceleration. We use 50 m as the reference depth of no motion (see discussion in section 7b). At stations with bottom depths shallower than 50 m, the geostrophic velocities at the ocean bottom are assumed to be zero. This means that the bottom pressure (dynamic height) at the shallower station is assumed to be equal to the pressure at the same depth (not the bottom pressure) of the nearby seaward station. The ageostrophic velocities $\mathbf{u}'$ are then derived by subtracting the calculated geostrophic velocities u^g, v^g from the total velocity u, v observed by ADCP, that is, $\mathbf{u}' = (u', v') = (u - u^g, v - v^g)$.

d. Generalized omega equation

In the QG theories, the vertical velocity w^g on the f plane can be derived from the **Q**-vector QG omega equation (Hoskins et al. 1978):

$$N^2\nabla_h^2 w^g + f^2 w^g zz = \underbrace{2\nabla_h \cdot \mathbf{Q}_h^g}_{S_{\text{DEFg}}}, \qquad (3)$$

where $N^2(z) = -\rho_0^{-1} g\overline{\rho_z}$ is the squared Brunt–Väisälä frequency, f is the Coriolis parameter, and $\mathbf{Q}_h^g \equiv \nabla_h \mathbf{u}^g \cdot \nabla_h \varrho$ is the horizontal geostrophic frontogenetical **Q** vector, in which $\mathbf{u}^g = (u^g, v^g)$ is the horizontal geostrophic velocity vector. The right-hand side of Eq. (3) is dynamically defined as geostrophic kinematic deformation term S_{DEFg}.

For a flow with a high Rossby number, a higher-order generalized omega equation for an inviscid, isentropic, and Boussinesq flow on the f plane is in the form of (Viúdez et al. 1996; Pallàs-Sanz and Viúdez 2005)

$$d\zeta'_z/dt = -f^{-1}\nabla_h \cdot (2\mathbf{Q}_h + \varrho_z\nabla_h W)$$
$$+ (f + \zeta)W_{zz} + \boldsymbol{\zeta}'_{ph_z} \cdot \nabla_h W - \boldsymbol{\zeta}'_{ph} \cdot \nabla_h^2 \mathbf{u}_h, \qquad (4)$$

where W is the vertical velocity, $\mathbf{Q}_h \equiv \nabla_h \mathbf{u}_h \cdot \nabla_h \varrho$ is the total **Q** vector, $\boldsymbol{\zeta}'_{ph} = (-v'_z, u'_z)$ is the horizontal ageostrophic pseudovorticity, $\mathbf{u}'_h = (u', v') = \mathbf{u}_h - \mathbf{u}_h^g$ is the ageostrophic horizontal velocities, and $\zeta'_z = \zeta_z - \zeta_z^g$ is the differential vertical vorticity of horizontal velocity $[\zeta_z = (v_x - u_y)_z]$ minus the differential geostrophic vorticity $[\zeta_z^g = (v_x^g - u_x^g)_z]$. Neglecting (i) the material rate of the change in ζ'_z, (ii) terms $\boldsymbol{\zeta}'_{ph_z} \cdot \nabla_h W$ and $\nabla_h\varrho_z \cdot \nabla_h W$, and (iii) the horizontal change in ϱ, the generalized omega equation [Eq. (4)] is simplified to

$$N^2\nabla_h^2 W + f(f + \zeta)W_{zz} = \underbrace{2\nabla_h \cdot \mathbf{Q}_h}_{S_{\text{DEF}}} + \underbrace{f\boldsymbol{\zeta}'_{ph} \cdot \nabla_h^2\mathbf{u}_h}_{S_{\text{ADV}}}. \qquad (5)$$

FIG. 2. Sea surface wind (white arrows, m s^{-1}) and SST (color, °C) fields on 13 and 18 Jul 2012 during the cruise observations. Landmarks QL and BO are labeled on the map for reference.

The first term on the right-hand side is total kinetic deformation S_{DEF}, which includes the geostrophic component S_{DEFg} in Eq. (3) and ageostrophic deformation S_{DEFa} $[S_{\text{DEFa}} = 2\nabla_h \cdot \mathbf{Q}'_h = 2\nabla_h \cdot (\nabla_h\mathbf{u}' \cdot \nabla_h\varrho)]$. The second term is the ageostrophic advection term S_{ADV}.

Further, taking the momentum and buoyancy turbulent flux induced by the vertical mixing into account, the generalized omega equation [Eq. (5)] has two more terms (Pallàs-Sanz et al. 2010b):

$$N^2\nabla_h^2 W + f(f + \zeta)W_{zz} = \underbrace{2\nabla_h \cdot \mathbf{Q}_h}_{S_{\text{DEF}}} + \underbrace{f\boldsymbol{\zeta}'_{ph} \cdot \nabla_h^2\mathbf{u}_h}_{S_{\text{ADV}}} + \underbrace{\underbrace{(f\boldsymbol{\zeta}_{ph} \cdot \nabla_h A_v - A_v\zeta_z)_{zz}}_{S_{\text{MOM}}} \underbrace{- [\nabla_h^2(K_v\varrho_z)]_z}_{S_{\text{BUO}}}}_{S_{\text{MIX}}}, \qquad (6)$$

where $\boldsymbol{\zeta}_{ph} = (-v_z, u_z)$ is the horizontal pseudovorticity vector, S_{MOM} and S_{BUO} are the vertical mixing fluxes of momentum and buoyancy, and K_v and A_v are the vertical eddy diffusivity and the vertical eddy viscosity, respectively.
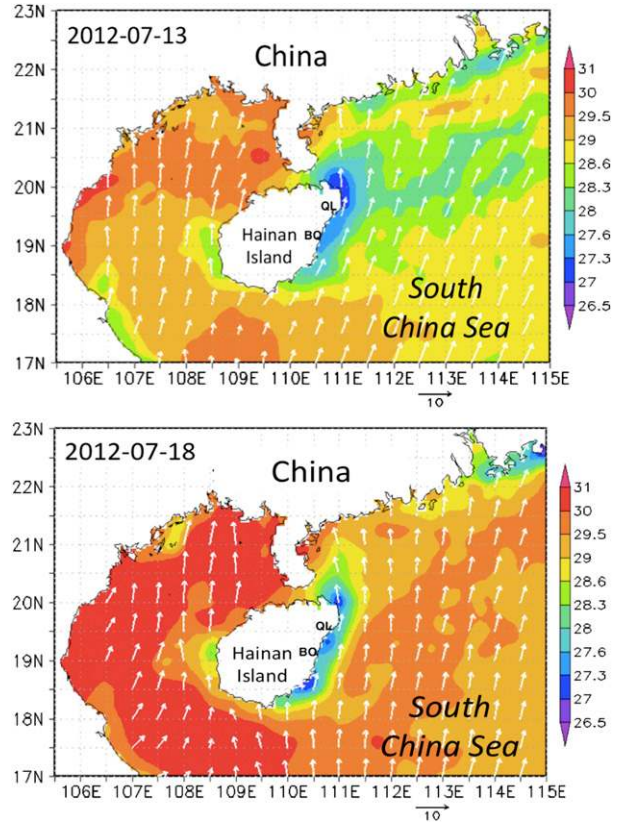
3. 3D density and velocity fields

a. Sea surface wind and sea surface temperature fields

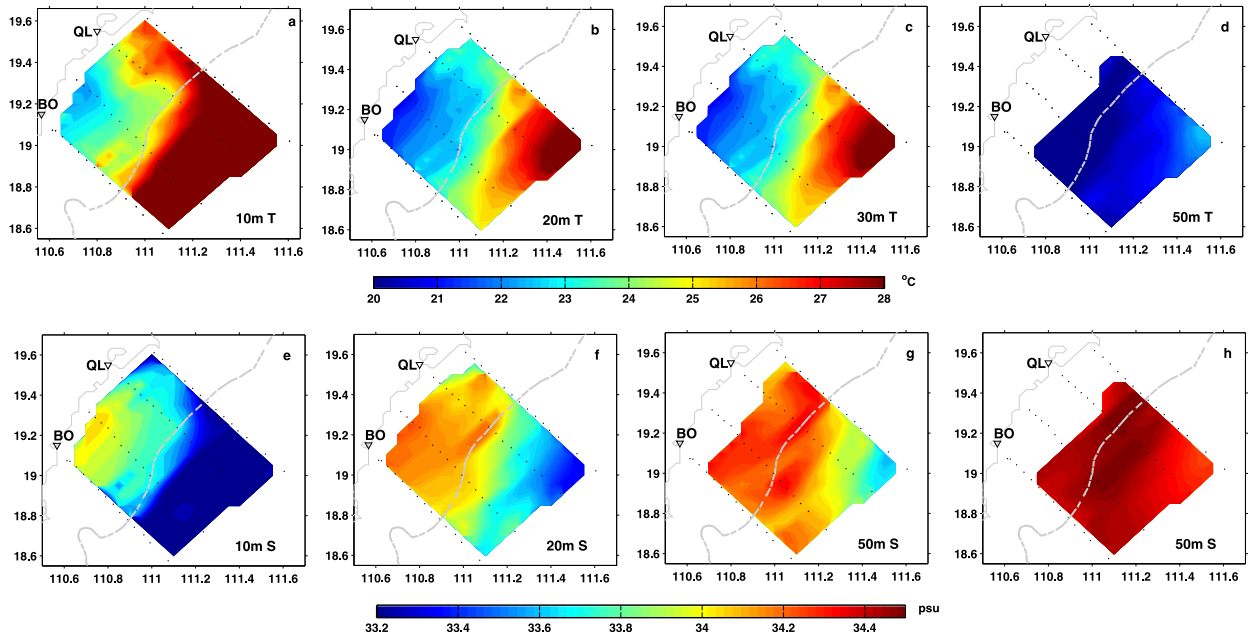Figure 2 shows the sea surface temperature (SST) and the surface wind fields on 13 and 18 July 2012 in the

FIG. 3. Horizontal (*x*–*y*) distribution maps of the (a)–(d) observed temperature T (°C) and (e)–(h) salinity S (psu) at 10, 20, 30, and 50 m. Landmarks QL and BO are labeled on the map for reference. Black dots represent the observation stations. Gray dashed lines represent the 100-m isobath.

northern SCS during the cruise observation. The SST data are $6 \times 6\,km^2$ daily products downloaded from website of the Group for High Resolution Sea Surface Temperature (GHRSST) project (http://data.nodc.noaa.gov/ghrsst/L4/GLOB/UKMO/OSTIA/). They are merged

products with in situ, microwave, and infrared satellite SSTs produced by the U.K. Meteorological Office. The wind data are downloaded f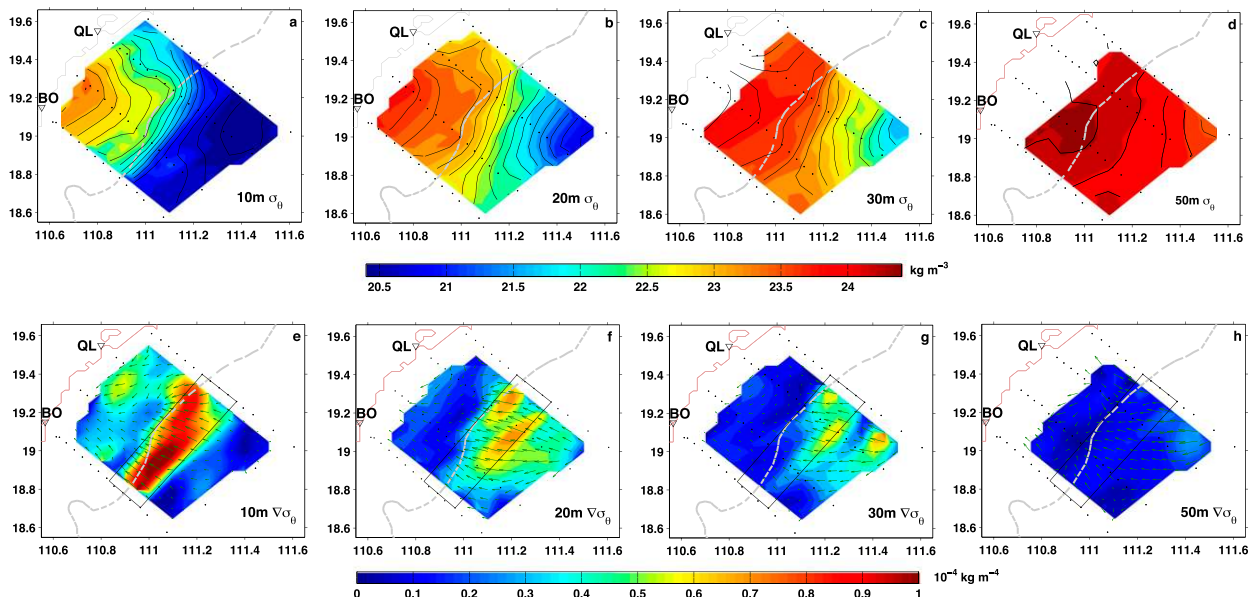rom the NOAA National Climatic Data Center (NCDC) website (ftp://eclipse.ncdc.noaa.gov/pub/seawinds/), which are derived from

FIG. 4. As in Fig. 3, but for the (a)–(d) potential density σ_θ (kg m^{-3}) and the (e)–(h) horizontal gradient of potential density $\nabla\sigma_\theta$ (10^{-4} kg m^{-4}). Black lines in (a)–(d) represent the isopycnals after the Gaussian filter (contour interval is 0.2 kg m^{-3}; $\sigma_{\theta\min} = 20.6, 21.0, 21.8$, and 23.8 kg m^{-3} at 10, 20, 30, and 50 m, respectively). Arrows in (e)–(h) represent the vector $\nabla\sigma_\theta$. Gray dashed lines represent the 100-m isobath. Black boxes represent the frontal zone.
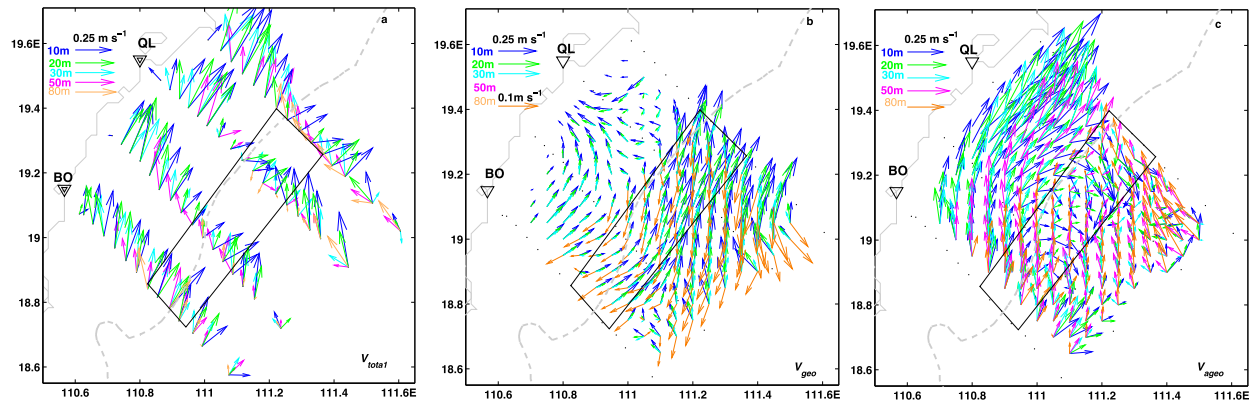
FIG. 5. Distribution maps of (a) the total horizontal velocity $\mathbf{V}_{total}$ observed by the ADCP, the (b) geostrophic velocity referred to 50 m $\mathbf{V}_{geo}$, and the (c) ageostrophic velocity $\mathbf{V}_{ageo} = \mathbf{V}_{total} - \mathbf{V}_{geo}$ at 10, 20, 30, 50, and 80 m. Gray dashed lines represent the 100-m isobath. Black boxes represent the frontal zone.

blended multiple satellite measurements of the Special Sensor Microwave Imager (SSM/I), the Tropical Rainfall Measuring Mission (TRMM) Microwave Imager (TMI), and the Advanced Microwave Scanning Radiometer for Earth Observing System (AMSR-E) at a 0.25° resolution.

As shown in Fig. 2, southerly winds prevailed during the observation period. This wind condition favors the coastal upwelling along the eastern coast of Hainan Island, China, which is characterized by cold water with SST lower than 28°C. The upwelling hugging the coast between the Qinglan (QL) Bay and Boao (BO) Bay is robust during the whole period, while the background temperature far offshore in the deeper SCS increases from about 29°C on 13 July to above 30°C on 18 July 2012.

b. Temperature, salinity, and density fields

Figure 3 shows the horizontal distribution maps of the water temperature and salinity at depths 10, 20, 30, and 50 m. One can see that the water of low temperature (<24°C) and high salinity (>34 psu) exists in the subsurface layer along the coast from BO to QL. An upwelling center with the temperature 5°C lower and the salinity 1 psu higher than that in the deep water appears near BO at depths above 30 m. This low-temperature and high-salinity upwelling center extends eastward and northward with the depth increased. The coastal waters north of QL are 1°C warmer and 0.2 psu fresher than that near BO.

From Fig. 4, one can see that the potential density increases 2.0–4.0 kg m^{-3} shoreward from the ocean area deeper than 100 m to near the coast. At 10 m, a strong density front with a maximum gradient of 1×10^{-4} kg m^{-4} appears along the 100-m isobath,

which separates the coastal upwelling dense water from the deep-ocean light water. Another weaker front with a gradient of 0.6×10^{-4} kg m^{-4} appears in the coastal water near QL, where the density is about 1 kg m^{-3} lower than the maximum potential density of 23.5 kg m^{-3} near BO. In the deeper layer, the upwelling dense water extends northward. The frontal zone is divided into more than two bands with the maximum gradient of 0.7×10^{-4} kg m^{-4} appearing in the northeastern observation area. Below 50 m, the density gradient becomes smaller than 0.2×10^{-4} kg m^{-4} with relatively large value in the deep-ocean area.

c. Horizontal velocity field and vorticity

Figure 5a shows the total horizontal velocities $\mathbf{V}_{total}$ observed by ADCP. One can see that the most velocity vectors at the upper 20 m are directing northeastward and generally parallel to the coastal line. The larger velocities appear near the coast with a maximum value of about 0.4 m s^{-1}. The velocity direction turns anticlockwise and the magnitudes decrease with the depth. Near the bottom, the flows generally turn shoreward in the ocean area deeper than 100 m, transporting deep-ocean waters shoreward. Figure 5b shows the geostrophic velocities $\mathbf{V}_{geo}$ referred to 50 m derived from the gridded densities and the thermal wind balance. One can see that the geostrophic velocities in the water deeper than 100 m are mostly northeastward with a maximum value of 0.4 m s^{-1} at the upper layer. Their amplitudes decrease to zero at the reference depth of 50 m, and the directions turn to southwestward in the deeper layer. The maximum southwestward geostrophic current is about 0.1 m s^{-1} at 80 m. In the shallow waters near the coast, the geostrophic velocities are smaller than 0.1 m s^{-1} and directing shoreward near QL.
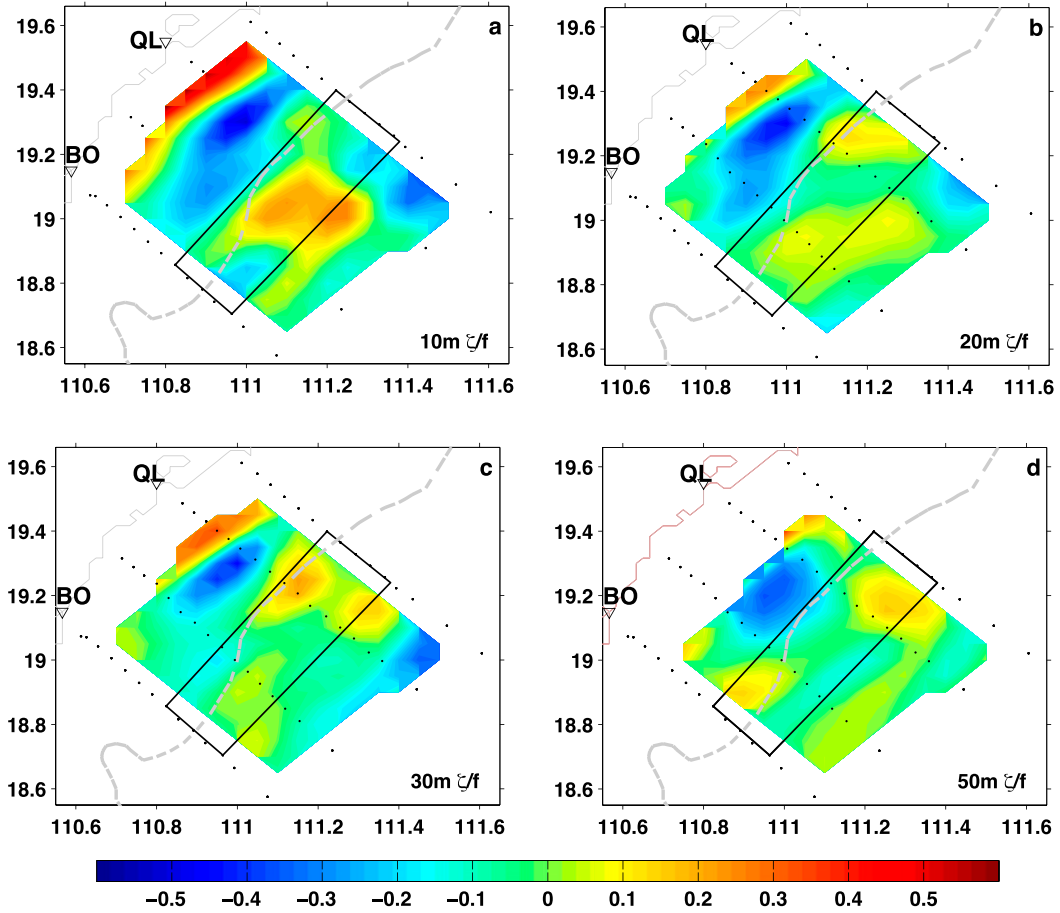
FIG. 6. As in Fig. 3, but for the scaled relative vorticity ζ/f.

Figure 5c shows the ageostrophic velocities calculated by subtracting the geostrophic velocities from the total velocities, that is, $\mathbf{V}_{\mathrm{ageo}} = \mathbf{V}_{\mathrm{total}} - \mathbf{V}_{\mathrm{geo}}$. One can see that the ageostrophic velocities near the coast are larger than $0.3\,\mathrm{m\,s}^{-1}$ and directing northeastward along the coast like the total velocities, indicating that the ageostrophic component has larger contribution to the total velocity in the shallow coastal water. In the deep water outside the front zone, the ageostrophic velocities are smaller than that in the coastal water and mainly directing shoreward below 50 m, implying the onshore transport supporting the coastal upwelling.

Figure 6 shows the scaled relative vorticity ζ/f (also named the Rossby number) derived from the total velocity field. One can see that it has larger values with a maximum/minimum of ±0.6 in the coastal water shallower than 100 m, indicating that ageostrophic advection should be considered in the dynamic analysis of the coastal water. In the deep ocean outside the front zone, the scaled relative vorticity is generally smaller than 0.2, so that QG effects may become important. These results

coincide with that from the ageostrophic velocities shown in Fig. 5c. Furthermore, the positive and negative vorticities appear alternatingly in the cross-shelf direction, similar to patterns of alternating large and small density gradients shown in Fig. 4.

d. Vertical mixing coefficient

The turbulent dissipation rate ε and the vertical eddy diffusivity K_v derived from the cruise microstructure observations are shown in Fig. 7. One can see that ε has a maximum value of $4 \times 10^{-7}\,\mathrm{W\,kg}^{-1}$ at 10 m, which appears on the seaward side of the frontal zone. In the frontal zone along the 100-m isobath, ε is generally one order of magnitude smaller than that on its two sides. In the cross-shelf direction, alternating smaller and larger ε bands appear as banded structure. The term ε dramatically decreases with the depth to smaller than $2.5 \times 10^{-9}\,\mathrm{W\,kg}^{-1}$ at 50 m. The banded structure persists in the deep layers with smaller ε on the shoreward side of the frontal zone along the 100-m isobath. The distribution of K_v mainly follows that of ε due to relatively
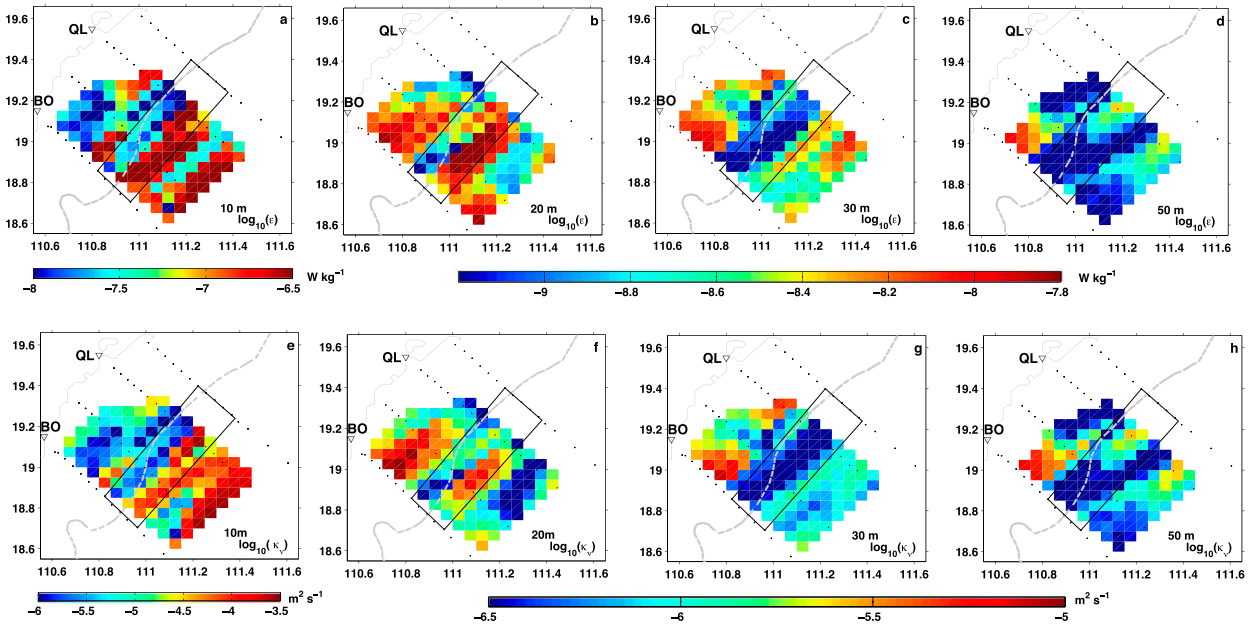
FIG. 7. As in Fig. 3, but for the (a)–(d) turbulent dissipation rate $\log_{10}(\varepsilon)$ (W kg^{-1}) and the (e)–(h) eddy diffusivity $\log_{10}(K_v)$ (m^2 s^{-1}). Color scale is logarithmic.

uniform Brunt–Väisälä frequency (not shown). At 10 m, K_v is smaller than 1×10^{-5} m^2 s^{-1} along the 100-m isobath and jumps to 1×10^{-4} m^2 s^{-1} on the seaward side of the frontal zone. The maximum value of $K_v = 3 \times 10^{-4}$ m^2 s^{-1} appears in the deep water outside the front zone, where the mixed layer is deeper than 10 m. The vertical eddy diffusivity K_v is generally smaller than 1×10^{-5} m^2 s^{-1} at water depths below 20 m, as shown in Figs. 7f–h. The mixed layer depths are shallower than 20 m at all stations in the study area. The weak mixing in layers below 20 m results from strong stratification with the Brunt–Väisälä frequency larger than 5×10^{-1} s^{-1}. In the cross-shelf direction, alternating large and small alongshore bands of K_v appear at all layers.

4. Dynamic terms of the generalized omega equation

a. Kinematic deformation term

Figures 8a–d show the horizontal distribution maps of the kinematic deformation term S_{DEF} ($2\nabla_h \cdot \mathbf{Q}_h$), which is derived from the observed total horizontal velocity and density at depths 10, 20, 30, and 50 m. One can see that S_{DEF} appears as alternating positive and negative alongshore bands with the maximum absolute values of 30×10^{-16} m^{-1} s^{-3} at 10 m near the 100-m isobath. At 20 m, the distribution pattern of S_{DEF} is similar to that at 10 m, but the maximum absolute value decreases to 20×10^{-16} m^{-1} s^{-3} near the 100-m isobath and smaller than 10×10^{-16} m^{-1} s^{-3} on the shoreward

side. Though the values of S_{DEF} decrease with the depth, the dominant banded structures are the same, that is, alternating positive and negative alongshore bands with a horizontal length scale of about 20 km.

We further calculate the geostrophic and ageostrophic components of the deformation term S_{DEFg} and S_{DEFa} from the calculated geostrophic and ageostrophic velocities. The results indicate that S_{DEFa} is generally larger than S_{DEFg} at all layers and has larger values in the shallow waters near the coast and the frontal zone. The banded distribution of S_{DEF} is dominated by S_{DEFa}, indicating the significant contribution of the ageostrophic deformation.

b. Ageostrophic advection term

The ageostrophic advection term S_{ADV} is related to the ageostrophic pseudovorticity vector $\boldsymbol{\zeta}'_{ph}$ and the Laplacian of $\mathbf{u}_h$ ($f\boldsymbol{\zeta}'_{ph} \cdot \nabla_h^2 \mathbf{u}_h$). We do not calculate $\boldsymbol{\zeta}'_{ph}$ directly from the ageostrophic velocity but derive it from the total pseudovorticity vector and the horizontal buoyancy gradient, that is, $f\boldsymbol{\zeta}'_{ph} = f\boldsymbol{\zeta}_{ph} - f\boldsymbol{\zeta}^g_{ph} = f\boldsymbol{\zeta}_{ph} - \nabla_h\varrho$. Figure 9 shows the distribution maps of ageostrophic advection term S_{ADV} at 10, 20, 30, and 50 m. One can see that S_{ADV} has alternating positive and negative bands with values above 30×10^{-16} m^{-1} s^{-3} at 10 m. The values of S_{ADV} decrease with the depth to about 10×10^{-16} m^{-1} s^{-3} below 20 m. The positive bands of S_{ADV} are always accompanied by the negative bands, supporting the banded structure. Comparing to kinematic deformation term S_{DEF} shown in Fig. 8, ageostrophic
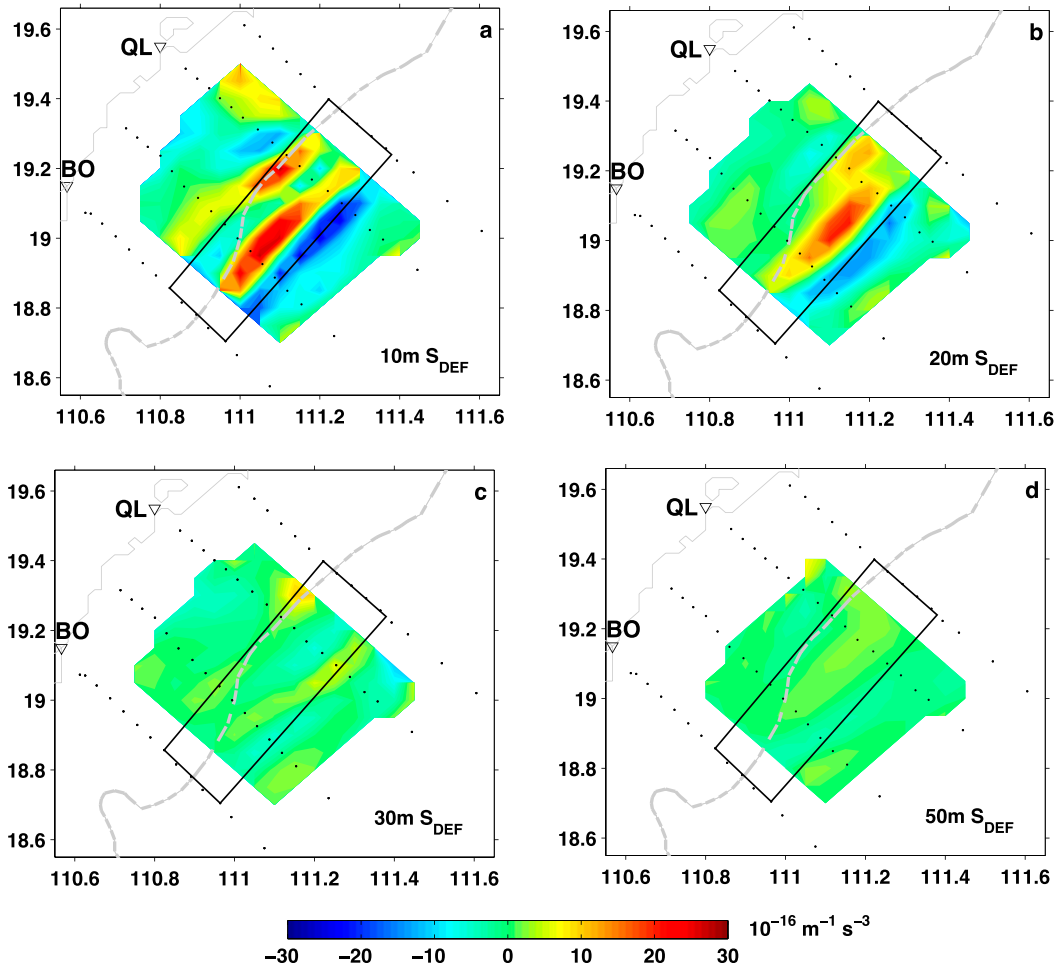
FIG. 8. Distribution maps of kinematic deformation term S_{DEF} ($10^{-16}\,\mathrm{m^{-1}\,s^{-3}}$) at (a) 10, (b) 20, (c) 30, and (d) 50 m. Gray dashed lines represent the 100-m isobath. Black dots represent the observation stations. Black boxes represent the frontal zone.

advection term S_{ADV} has larger values in the shallow waters and smaller values near the 100-m isobath. They counteract each other with similar values but opposite signs.

c. Vertical mixing forcing term

Taking the Prandtl number to be 1 and the vertical eddy coefficient A_v equal to the diffusivity K_v shown in Figs. 7e–h, the vertical mixing (S_{MIX}) of momentum flux term S_{MOM} $[(f\boldsymbol{\zeta}_{ph} \cdot \nabla_h A_v - A_v \zeta_z)_{zz}]$ and buoyancy flux term S_{BUO} $\{[\nabla_h^2 (K_v \varrho_z)]_z\}$ can be derived from the observations. As shown in Fig. 10, S_{MOM} has the largest value of $10 \times 10^{-16}\,\mathrm{m^{-1}\,s^{-3}}$ at 10 m in the frontal zone, where the upper mixed layer depths are about 5–9 m and the eddy diffusivity varies significantly from the mixed layer to the thermocline. The maximum value of S_{MOM} decreases rapidly to $2 \times 10^{-16}\,\mathrm{m^{-1}\,s^{-3}}$ at 20 m and $0.05 \times 10^{-16}\,\mathrm{m^{-1}\,s^{-3}}$ below 30 m, which is one to two

orders of magnitude smaller than that of S_{DEF} and S_{ADV}. The buoyancy flux term S_{BUO} is larger than S_{MOM} at 10 m and has the maximum value of $20 \times 10^{-16}\,\mathrm{m^{-1}\,s^{-3}}$ in the frontal zone. It also rapidly decreases with the depth and has a maximum value of about $0.5 \times 10^{-16}\,\mathrm{m^{-1}\,s^{-3}}$ at 20 m, smaller than that of S_{MOM}. At depths below 30 m, the values of S_{BUO} are smaller than $0.05 \times 10^{-16}\,\mathrm{m^{-1}\,s^{-3}}$. The distribution patterns of S_{MOM} and S_{BUO} are also featured by the banded structure, following that of the eddy diffusivity K_v. The signs of S_{MOM} and S_{BUO} bands are mostly opposite.

Figure 11 shows the total vertical mixing forcing term S_{MIX} ($=S_{MOM} + S_{BUO}$) at 10, 20, 30, and 50 m. One can see that S_{MIX} is also featured by the banded structure similar to that of S_{MOM} and S_{BUO}. At 10 m, S_{MIX} has similar distribution patterns and values to that of S_{BUO}. Its largest value $20 \times 10^{-16}\,\mathrm{m^{-1}\,s^{-3}}$, comparable to that of S_{DEF} and S_{ADV}, appears in the frontal zone near
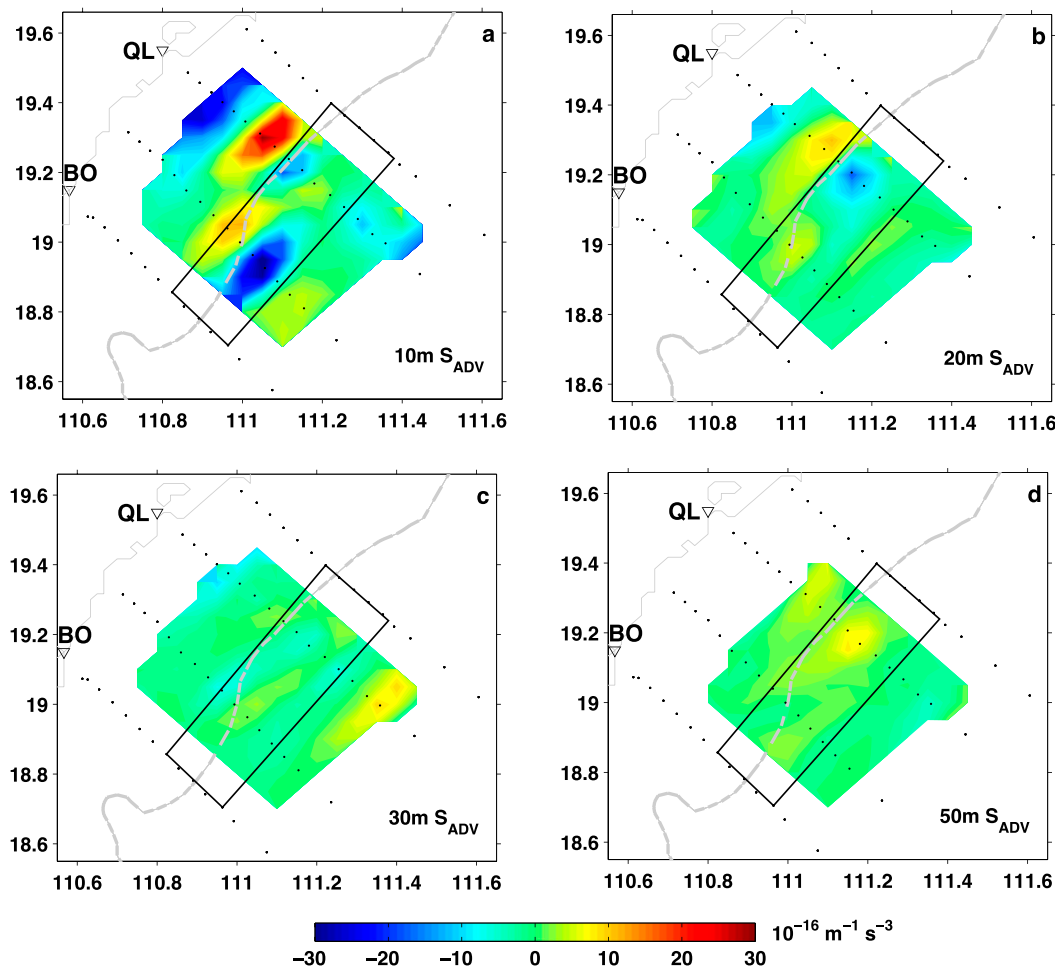
FIG. 9. As in Fig. 8, but for the ageostrophic advection term S_{ADV}.

the 100-m isobath. At 20 m, the largest value of S_{MIX} decreases by an order of magnitude to $-2 \times 10^{-16}\,\mathrm{m}^{-1}\,\mathrm{s}^{-3}$ at the deepest stations, which is dominated by S_{MOM}. In the deeper layers, S_{MIX} decreases to smaller than $0.1 \times 10^{-16}\,\mathrm{m}^{-1}\,\mathrm{s}^{-3}$. The values of the total mixing forcing term S_{MIX} are one to two orders of magnitude smaller than that of S_{DEF} and S_{ADV} at depths below 20 m. This implies the limited effects of mixing on the vertical circulation in the upper ocean.

5. 3D vertical circulation

Assuming vertical velocity $W = 0$ at the surface, the ocean bottom, and the lateral boundaries, we derive the 3D structure of the vertical circulation from the cruise observations using the generalized omega equation [Eq. (6)]. In calculation, the S_{MIX} at grids in the northern study area without microstructure observations are extrapolated with the nearest values, so that the values of S_{DEF} and S_{ADV} at these grids can be used.

Figure 12 shows the calculation results of vertical velocities W under the effects of S_{DEF}, S_{ADV}, and S_{MIX}. One can see that a strong downwelling band with a maximum velocity of $-5 \times 10^{-5}\,\mathrm{m}\,\mathrm{s}^{-1}$ appears at 10 m in the frontal zone with concentrated isopycnals. An upwelling band with a maximum velocity of $5 \times 10^{-5}\,\mathrm{m}\,\mathrm{s}^{-1}$ appears in the lighter water on the seaward side of the frontal zone. In the shallow coastal water, stronger upwelling with a maximum velocity core of $7 \times 10^{-5}\,\mathrm{m}\,\mathrm{s}^{-1}$ dominates near QL, where the concentrated isopycnals are perpendicular to the coastline. The distribution patterns of alternatingly appearing upwelling and downwelling bands at 20, 30, and 50 m are similar to that at 10 m, while the maximum velocities decrease with the depth. Generally, the distribution of the vertical circulation also shows the banded structure as alternating upwelling and downwelling from the coast to the deep ocean.

Figure 13 shows the distribution of W along two cross-shelf sections H and F. One can see the positive and negative stripes of the vertical velocity alternatingly
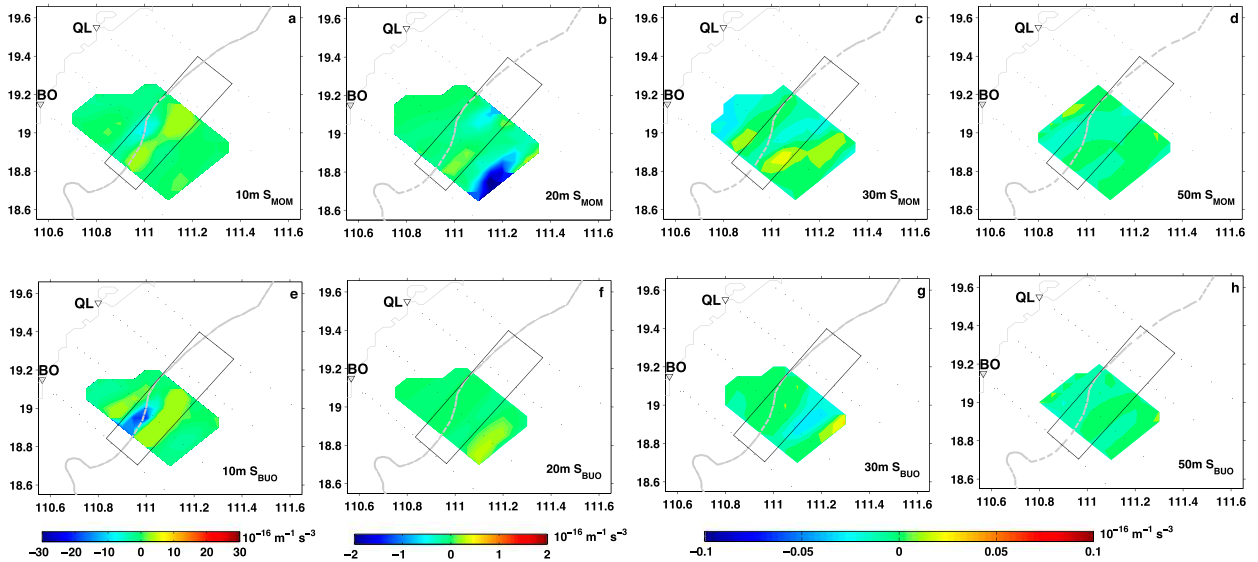
FIG. 10. As in Fig. 8, but for terms (a)–(d) S_{MOM} and (e)–(h) S_{BUO}.

appear along the sections. At section H, upwelling near the coast has the vertical velocity of about $2 \times 10^{-5}\,\text{m}\,\text{s}^{-1}$ at depths of 10–20 m. Downwelling with a maximum of $-3 \times 10^{-5}\,\text{m}\,\text{s}^{-1}$ appears at 10–20 m at stations in the frontal zone 40–60 km offshore, and upwelling with a maximum of about $4 \times 10^{-5}\,\text{m}\,\text{s}^{-1}$ appears at 10–40 m at stations outside the frontal zone 60–80 km offshore. At section F, the vertical velocity near the coast reaches $5 \times 10^{-5}\,\text{m}\,\text{s}^{-1}$, which is greater than that at section H. Another strong upwelling center with the vertical velocity larger than $4 \times 10^{-5}\,\text{m}\,\text{s}^{-1}$ appears at 5–30 m at stations outside the frontal zone 70 km offshore. Between the two strong upwelling centers, downwelling with maximum velocity of $-4 \times 10^{-5}\,\text{m}\,\text{s}^{-1}$ appears at 10–70 m in the frontal zone. In general, two sections of the vertical circulation show similar patterns. However, there are remarkable differences: 1) the vertical circulation at section F is stronger than that at section H, and 2) the downwelling band at section F is wider than that at section H. This reflects a northward-intensifying trend of upwelling and frontal zone.

We further calculate alongshore-averaged W and compare its cross-shelf variation with that of dynamic terms S_{DEF}, S_{ADV}, and S_{MIX}. The results at depths 10, 20, 30, and 50 m are shown in Figs. 14a–d. One can see that the alongshore-averaged W and all dynamic terms undulate along the cross-shelf direction with a horizontal length scale of $O(20–40)$ km. Above 30 m, S_{DEF}, which is dominated by its ageostrophic component S_{DEFa}, is the dominant dynamic term in deep waters, especially in the frontal zone and the nearby deep-ocean water at about 50–70 km from the coast. In the shallow waters within 40 km offshore, S_{ADV} becomes

the dominant term. At 50 m, the frontal zone weakens and S_{ADV} dominates most sections. The term S_{MIX} is dominated by S_{BUO} and is comparable to S_{DEF} and S_{ADV} at 10 m. It is dominated by S_{BUO} and is one order of magnitude smaller than S_{DEF} and S_{ADV} at 20 m. This term is two orders of magnitude smaller than S_{DEF} and S_{ADV} and negligible below 30 m. The variation of W follows that of S_{DEFa} and S_{ADV}. It always has two positive extrema: one is located in the shallow coastal water at 20 km offshore, and another is located in the deep ocean outside the frontal zone 70 km offshore. The maximum W is $2 \times 10^{-5}\,\text{m}\,\text{s}^{-1}$ at 10–20 m in the coastal upwelling region and $3 \times 10^{-5}\,\text{m}\,\text{s}^{-1}$ outside the frontal zone, respectively.

6. Discussion

a. Mechanism of banded structure of the vertical velocity

Previous investigators have found banded distribution of the forcing term and vertical velocity in the mesoscale and submesoscale fronts, where the vertical velocity is upward on the light (warm) side and downward on the heavy (cold) side (Capet et al. 2008; McWilliams 2016). In this study, the vertical circulation shows multiple bands in the cross-shelf direction, which has downwelling in the frontal zone, and upwelling on two sides of the frontal zone. This is a bit different from typical one upwelling–downwelling cell in the fronts but similar to the results by Thomas and Lee (2005) and Nagai et al. (2012), which show two or multiple cells of cross-frontal circulation forced by downfront wind stress. We suggest that the banded structure obtained
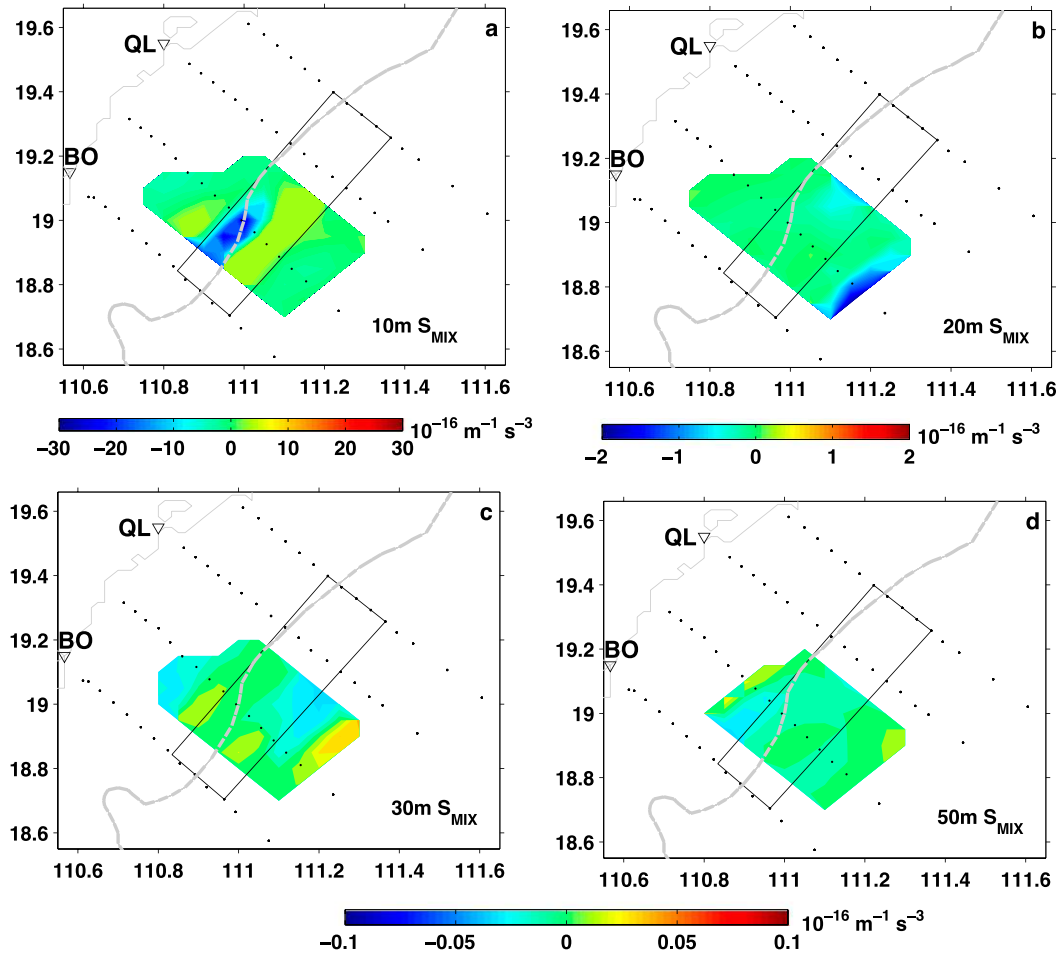
FIG. 11. As in Fig. 8, but for the total vertical mixing forcing term S_{MIX}.

by this study results from the coexistence of the frontal zone and coastal upwelling induced by wind-driven Ekman suctions.

According to Stern (1965) and Pallàs-Sanz et al. (2010a), the nonlinear Ekman transport $\mathbf{M}_e$ caused by the wind stress $\boldsymbol{\tau}_h$ interacting with a background flow is

$$\rho\mathbf{M}_e \simeq -\frac{\mathbf{k} \times \boldsymbol{\tau}_h}{f + \zeta_0}, \qquad (7)$$

and the total Ekman suctions W_e is

$$\rho W_e \simeq \frac{\mathbf{k}}{(f + \zeta_0)} \cdot \nabla_h \times \boldsymbol{\tau}_h + \frac{\mathbf{k} \times \boldsymbol{\tau}_h}{(f + \zeta_0)^2} \cdot \nabla_h(f + \zeta_0), \qquad (8)$$

where ζ_0 is the geostrophic vertical vorticity at the surface. The first term on the right-hand side of Eq. (8) is the classic linear Ekman pumping due to the wind curl. The second term represents the interaction

of the wind stress and perpendicular gradient of the vorticity. This indicates that the gradient of ζ_0 generates the vertical velocity even when the wind stress curl is zero. We use the averaged wind stress over 13–18 July 2012 for calculation. The results of $\mathbf{M}_e$ and W_e are shown in Fig. 15a. One can see that Ekman transport is mostly eastward with a magnitude of $O(1)\,\mathrm{m^2\,s^{-1}}$. The total Ekman suction, which is mainly induced by the interaction of the wind and the gradient of ζ_0, shows banded structure in the cross-shelf direction. Upwelling bands appear near the coast and outside the 100-m isobath with the maximum vertical velocity of 3×10^{-5} and $5 \times 10^{-5}\,\mathrm{m\,s^{-1}}$, respectively. Between the upwelling bands, downwelling dominates with a maximum velocity of $-5 \times 10^{-5}\,\mathrm{m\,s^{-1}}$.

The results of W_e are similar to the vertical velocity W_{SADV} only forced by the dynamic term S_{ADV} as shown in Fig. 15b. Wind influence is included implicitly in S_{ADV} through the ageostrophic vertical shear [Eq. (5)]. In this case, the ageostrophic currents
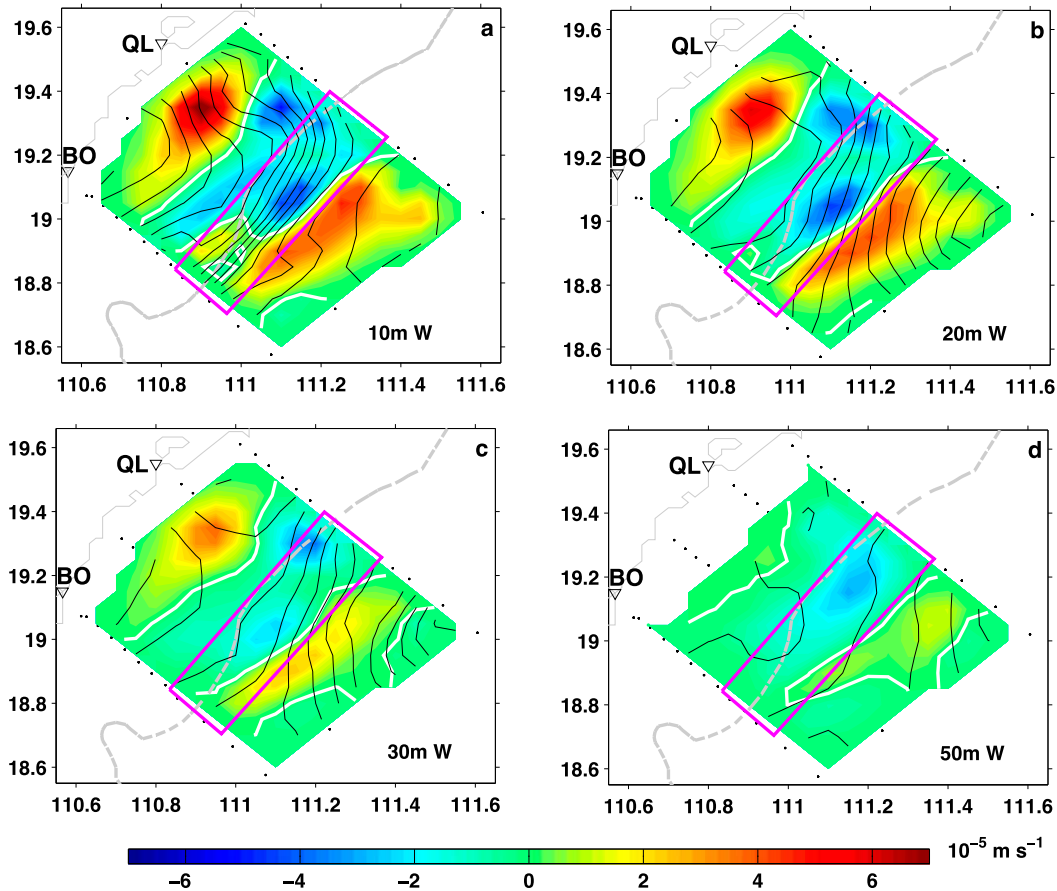
FIG. 12. Distribution maps of vertical velocity W (10^{-5} m s^{-1}) at (a) 10, (b) 20, (c) 30, and (d) 50 m. White lines represent the zero contour. Black lines represent the isopycnals in Figs. 4a–d. The gray line represents the 100-m isobath. Pink boxes represent the frontal zone.

are mainly related to the Ekman currents that are stronger near the coast. Thus, W_{SADV} dominates the total W near the coast, where the upwelling band appears as shown in Fig. 13.

b. Effects of mixing on the vertical circulation

Nagai et al. (2006) and Pallàs-Sanz et al. (2010b) investigated the effect of vertical mixing on the vertical circulation in ocean fronts using parameterized eddy viscosity due to the lack of observed mixing data. In this study, vertical mixing parameters are derived from direct measurements with the Turbulence Ocean Microstructure Acquisition Profiler (TurboMAP) and are included in the generalized omega equation for the first time. Our analysis shows that the mixing forcing term S_{MIX} is comparable to deformation and advection terms only at 10 m in the frontal zone but one to two orders of magnitude smaller at depths below 30 m. To test the effects of the mixing on the vertical circulation, we calculate the vertical velocity without S_{MIX}, that is, W_{nmix}. The results

show that W_{nmix} has similar distribution patterns and values as that of W at most stations and depths (not shown). Figures 16a–d show the difference between the vertical velocities with and without mixing forcing, that is, $\Delta W_{mix} = W - W_{nmix}$, at 10, 20, 30, and 50 m. One can see that the maximum of ΔW_{mix} reaches 2×10^{-5} m s^{-1} at 10 m in the frontal zone, which is about 30%–40% of the total W there. The maximum of ΔW_{mix} decreases rapidly to one order of magnitude smaller than W at 20 m and negligible below 30 m. As shown in Fig. 16e, the horizontal mean value of $|\Delta W_{mix}|$, that is, $|\Delta W_{mix}|_{xy}$, only has values larger than 0.5×10^{-6} m s^{-1}, that is, 10%–15% of $|W|_{xy}$ (at 5–30 m), with a maximum value at 10 m. Below 30 m, $|\Delta W_{mix}|_{xy}$ becomes two orders of magnitude smaller than $|W|_{xy}$. Compared to the distribution of the vertical eddy diffusivity shown in Fig. 16f, one can see that the larger $|\Delta W_{mix}|_{xy}$ in the upper 30-m layer corresponds to strong mixing with $|K_v|_{xy}$ larger than 3×10^{-6} m^2 s^{-1}. This is similar to that suggested by Nagai et al. (2006, 2008), that is, the influence of the vertical mixing on
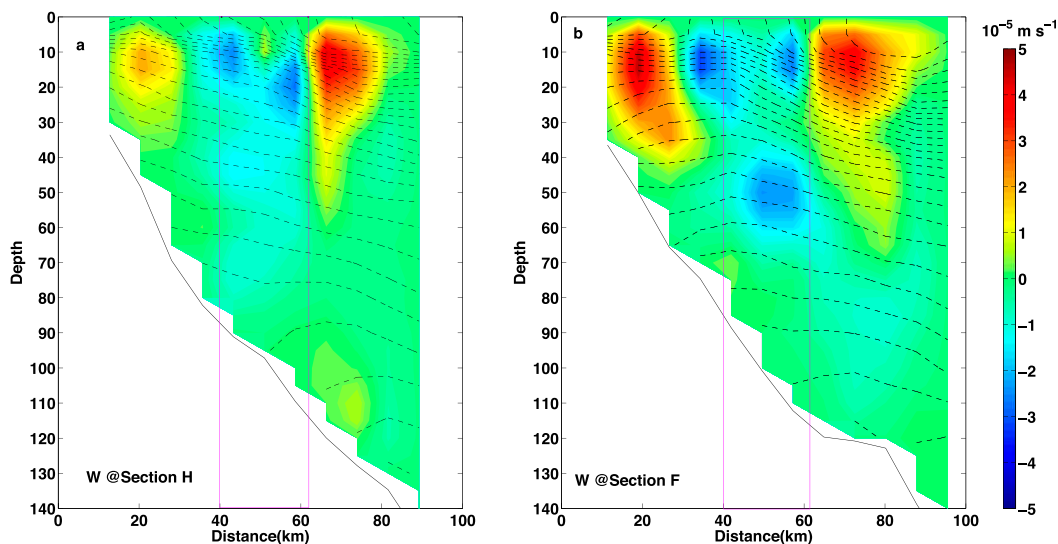
FIG. 13. Vertical distribution of vertical velocity W ($10^{-5}\,\mathrm{m\,s^{-1}}$) along sections (a) H and (b) F. Black lines represent the sea bottom. The isopycnals are shown as black dashed lines, $\sigma_{\theta\mathrm{min}} = 20.4\,\mathrm{kg\,m^{-3}}$; the contour interval is $0.2\,\mathrm{kg\,m^{-3}}$. Pink boxes represent the frontal zone.

vertical velocity may be important when the eddy diffusivity and the associated scaled Ekman number with deformation rate are large. Furthermore, the largest $|\Delta W_{\mathrm{mix}}|_{xy}$ appears at the depth where the vertical gradient of the eddy diffusivity $|\mathrm{grad}_z(K_v)|_{xy}$ is the largest, implying the vertical variation of the eddy diffusivity is also important to the vertical velocity.

The confined effects of mixing on the vertical velocity in the upper ocean derived from our observations, in general, are similar to the results estimated by Nagai et al. (2006) and Pallàs-Sanz et al. (2010b). However, contribution of vertical mixing to intensification of vertical velocity is not as great as predicted by previous studies. The reason is that cruise-observed eddy diffusivities in our case are smaller than the values estimated by the previous investigators (Nagai et al. 2006; Pallàs-Sanz et al. 2010b). In fact, as pointed out by Pallàs-Sanz et al. (2010b), the effects of vertical mixing on the vertical velocity are quite sensitive to the vertical mixing parameterization, and the intensification factor of the vertical velocity by mixing significantly decreases from 2 to 0.5 as the parameterized eddy viscosity decreases from 1×10^{-2} to $6 \times 10^{-3}\,\mathrm{m^2\,s^{-1}}$. In this study, the eddy diffusivities from observations have values smaller than $3 \times 10^{-4}\,\mathrm{m^2\,s^{-1}}$, which is one to two orders of magnitude smaller than the parameterized mixing coefficients used by the previous investigators. If the missed eddy diffusivities in the mixed layer are filled with values two orders of magnitude larger, the maximum ΔW_{mix} could reach $\pm 20 \times 10^{-5}\,\mathrm{m\,s^{-1}}$

at 10 m in the frontal zone, which is about 300%–400% of the vertical velocity without mixing.

c. Sensitivity of the vertical velocity to the geostrophic reference level

For calculation of geostrophic velocities, we use 50 m as the reference level of no motion. As shown in Fig. 5b, the directions of the resulted geostrophic velocities turn to southward at 80 m. The north component of the geostrophic velocities at section H shown in Fig. 17a also has negative values below 50 m, which is the opposite of the northward flow in the upper layer. This is consistent with the downward tilt of isopycnals toward the coast in the deep layer, indicating the choice of no motion at 50 m is feasible. We further calculate the geostrophic velocities and geostrophic and ageostrophic deformation terms with levels of no motion at 70 m and the ocean bottom for comparison. As shown in Figs. 17b and 17c, the patterns and values of the geostrophic velocities in the upper 40 m change little with reference levels changing from 50 m to the ocean bottom. Meanwhile, dynamic terms S_{DEFg} and S_{DEFa} in the upper layers are insensitive to the reference level, as in the example shown in Fig. 17d. One can see that below 70 m, the variation of S_{DEFg} and S_{DEFa} counteract with each other, making their sum unchanged. In fact, S_{DEF} is derived from the total velocity observed by ADCP in our calculation and is independent of the reference level.

For the vertical velocity derived from the omega equation, the forcing term is geostrophic deformation S_{DEFg} in QG assumption, which is determined by two
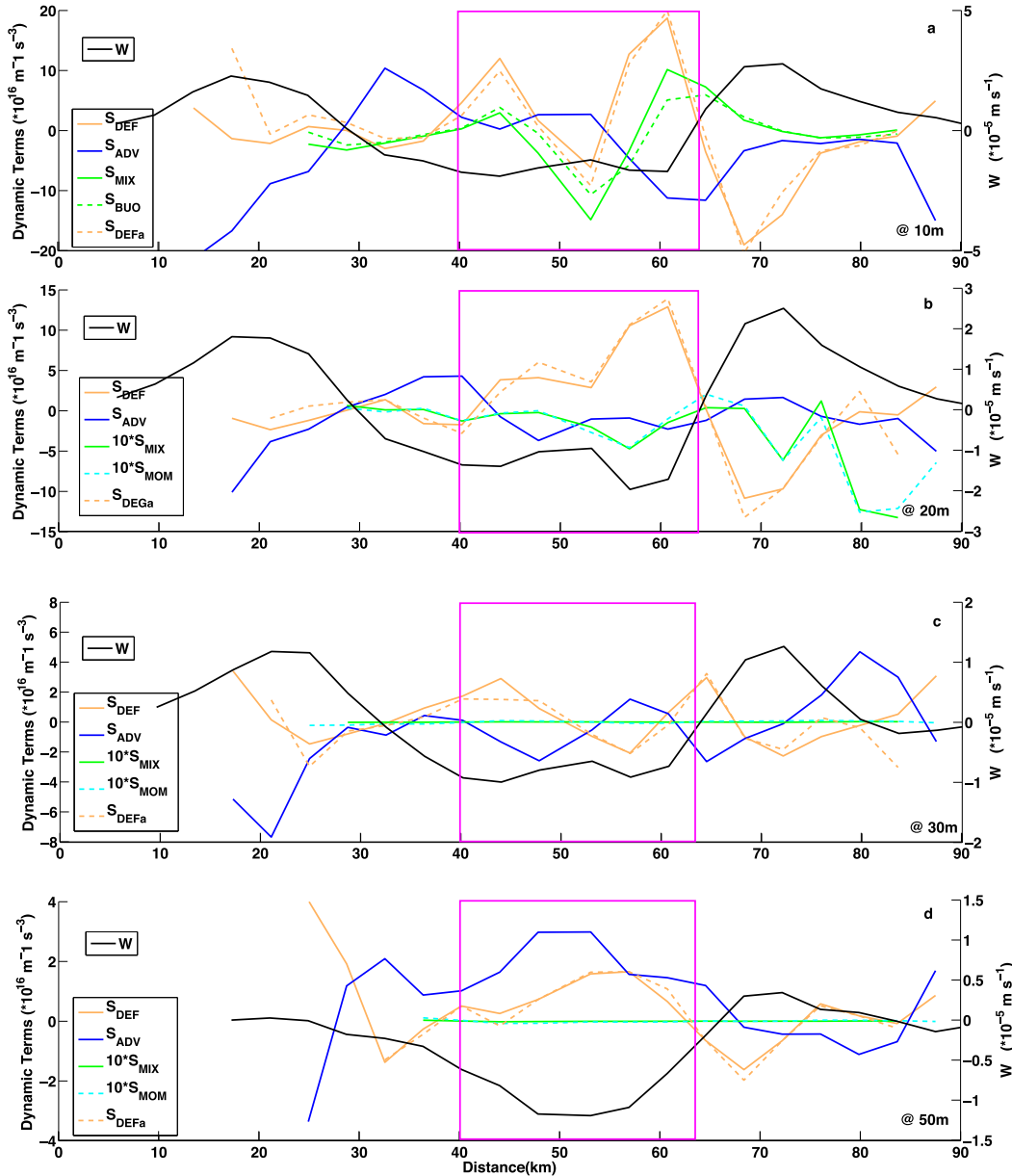
FIG. 14. Alongshore-averaged dynamic terms S_{DEF}, S_{ADV}, S_{MIX}, S_{MOM}, S_{BUO}, S_{DEFa}, and W in the cross-shelf direction at (a) 10, (b) 20, (c) 30, and (d) 50 m. Pink boxes represent the frontal zone.

key horizontal derivatives of the density and the geostrophic velocity (Hoskins et al. 1978). Thus, careful attention should be paid to the calculation of geostrophic velocities (Rudnick 1996). Different from the QG equation used by the previous investigators, in this study we use the generalized omega equation to calculate the vertical circulation. Forcing terms S_{DEF}, S_{ADV}, and S_{MIX} are derived from the in situ density measured by CTD, the eddy diffusivity measured by TurboMAP, and the total horizontal velocity measured by ADCP, instead of the calculated geostrophic velocity. The

ageostrophic component ζ'_{ph} is explicit in term S_{ADV}, but it is independent of the choice of geostrophic reference level because ζ'_{ph} is derived from the in situ density and the observed total velocity (i.e., $f\zeta'_{ph} = f\zeta_{ph} - \nabla_h \varrho$). Thus, in our case the selection of the geostrophic reference level has no effect on the final results of the vertical velocity.

d. Effects of bottom topography

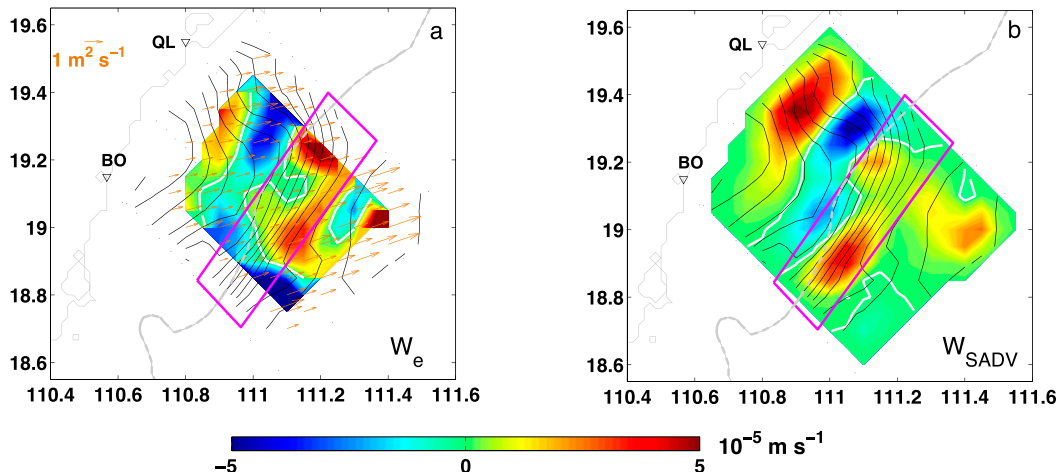In this study, we assume the vertical velocities at the ocean bottom as zero. To examine the dynamic effect of

FIG. 15. (a) Nonlinear Ekman transport $\mathbf{M}_e$ (arrows) and Ekman suction W_e (color, $10^{-5}\,\mathrm{m\,s^{-1}}$) and (b) vertical velocity W_{SADV} ($10^{-5}\,\mathrm{m\,s^{-1}}$) forced by S_{ADV} at 10 m. The potential density (black lines, $\sigma_{\theta min} = 20.6\,\mathrm{kg\,m^{-3}}$; contour interval is $0.2\,\mathrm{kg\,m^{-3}}$) at 10 m is shown. The gray dashed line represents the 100-m isobath. White lines represent the zero contours. Pink boxes represent the location of the frontal zone.

the bottom topography, we do numerical experiments using the kinetic boundary condition:

$$W = -\mathbf{u}_{bot} \cdot \nabla h = -u_{bot}\frac{\partial h}{\partial x} - v_{bot}\frac{\partial h}{\partial y} \quad \text{at} \quad z = -h, \quad (9)$$

Where u_{bot} and v_{bot} are the horizontal components of the total velocity at the ocean bottom and h is the bottom depth. At stations where the ADCP observations do not reach the bottom, u_{bot} and v_{bot} are assumed to be

the same as that at the deepest observed depth bin, which are mostly about 0.05–0.15 m s^{-1}.

Figures 18a–d show the vertical velocity with the kinetic boundary, that is, W_{kb}, at 10, 20, 30, and 50 m. One can see that W_{kb} at 10 m has values and banded distribution patterns of alternating upwelling and downwelling bands quite close to that of W shown in Fig. 12. Below 10 m, W_{kb} still has similar banded structure in the cross-shelf direction, but the maximum values of the upwelling and
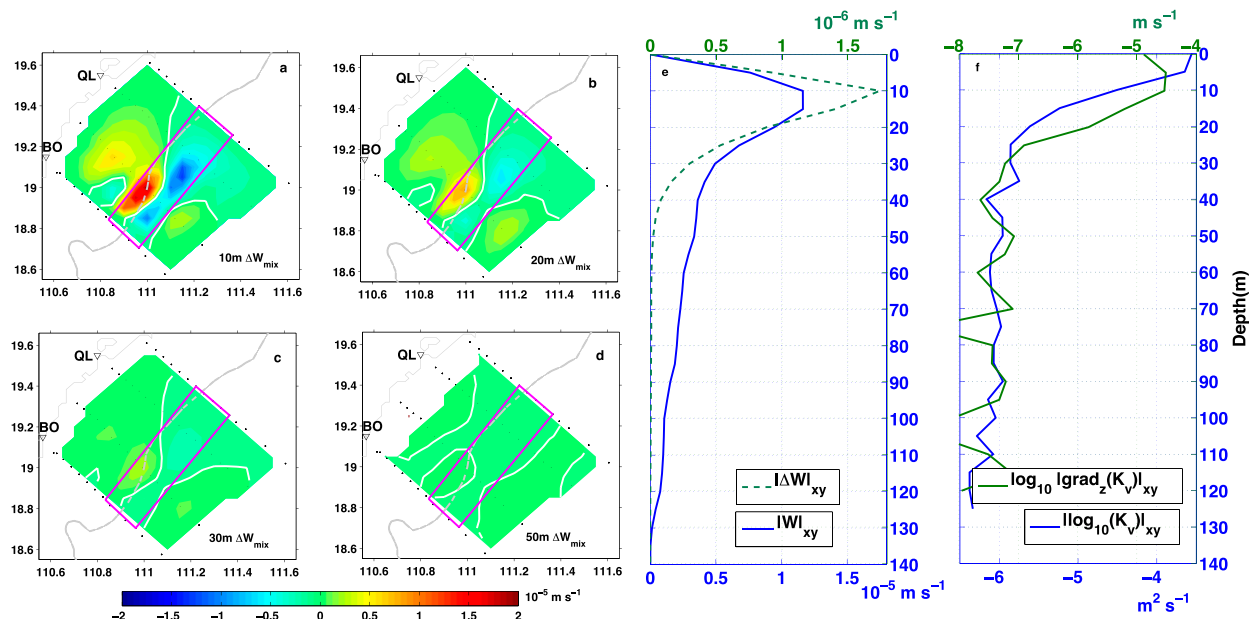

FIG. 16. Distribution maps of difference ΔW_{mix} between vertical velocities with and without mixing forcing at (a) 10, (b) 20, (c) 30, and (d) 50 m. (e) Vertical distribution of horizontally averaged $|\Delta W_{mix}|_{xy}$ (green) and $|W|_{xy}$ (blue). (f) Vertical distribution of horizontally averaged eddy diffusivity $|\log_{10}(K_v)|_{xy}$ (blue) and its vertical gradient $\log_{10}|\mathrm{grad}_z(K_v)|_{xy}$ (green). Gray dashed lines in (a)–(d) represent the 100-m isobath. White lines represent the zero contours. Pink boxes represent the frontal zone.
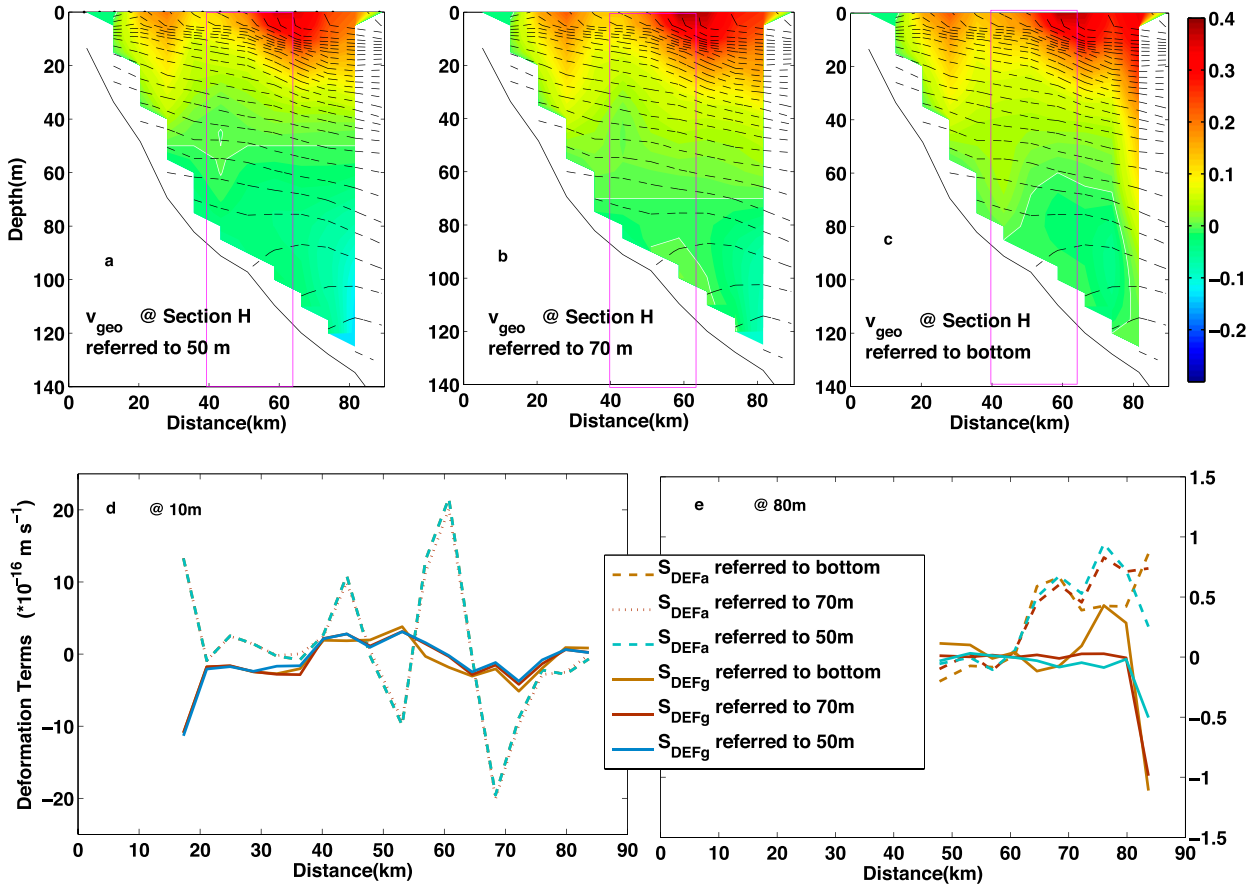
FIG. 17. Northward component of geostrophic velocities (m s^{-1}) referred to (a) 50 m, (b) 70 m, and the (c) ocean bottom. Alongshore-averaged S_{DEFg} and S_{DEFa} at (d) 10 and (e) 80 m. White lines in (a)–(c) represent the zero contours.

downwelling become larger than that of W, especially in the shallow waters near the coast. As shown in Figs. 18e–h, the difference between W_{kb} and W, that is, $\Delta W_{bot} = W_{kb} - W$, in the upwelling bands near the coast increases significantly with the depth from about 0.5×10^{-5} m s^{-1}, 10% of W_{kb}, at 10 m to larger than 3×10^{-5} m s^{-1}, 50% of W_{kb}, at 50 m. In the frontal zone and the seaward deep water, the maximum ΔW_{bot} is only about 1×10^{-5} m s^{-1} appearing at 20 and 30 m, about 15%–20% of W_{kb}. The signs of ΔW_{bot} are coherent with that of W_{kb}. The maximum ΔW_{bot} appears in the deeper layer on the edge of the upwelling bands near the coast, where W is close to zero under no-slip boundary condition. This implies that the effect of the bottom topography on the vertical circulation is evident in the deep layer when the kinetic boundary condition with bottom horizontal velocities larger than 0.05 m s^{-1} is used in the study area.

e. Of low-frequency contamination

In this study, the total horizontal velocities used for vertical velocity calculation have been averaged from 5–50-min ADCP observations to eliminate high-frequency variations. However, random, low-frequency contamination might still be contained. In coastal oceans, tidal currents are usually the strongest components to contaminate the total velocity. Previous long-time observations have shown that the tidal currents are smaller than 0.1 m s^{-1} in the shelf water near our study area (Xu et al. 2011; He et al. 2012). We observed the maximum velocity amplitudes of K_1 and M_2 tides in the study area during other cruise projects. The results are 0.15 m s^{-1} in the upper layer and smaller than 0.05 m s^{-1} in the deep water. The horizontal scale of the tidal ellipse is of $O(10)$ km. Thus, in order to remove the tidal contamination, we preprocess the cruise-observed data with a 2D Gaussian filter of 35×25 km^2 prior to calculating the vertical velocities. The near-inertial oscillations (NIOs) are another potential contamination factor. However, the NIOs occur as an episodic event due to the sudden variation of strong wind. The strong signals of NIOs only occur spatially within an ocean area near the ground track and temporally within a week after the passage of a hurricane (or typhoon or storm; Zheng et al. 2006;
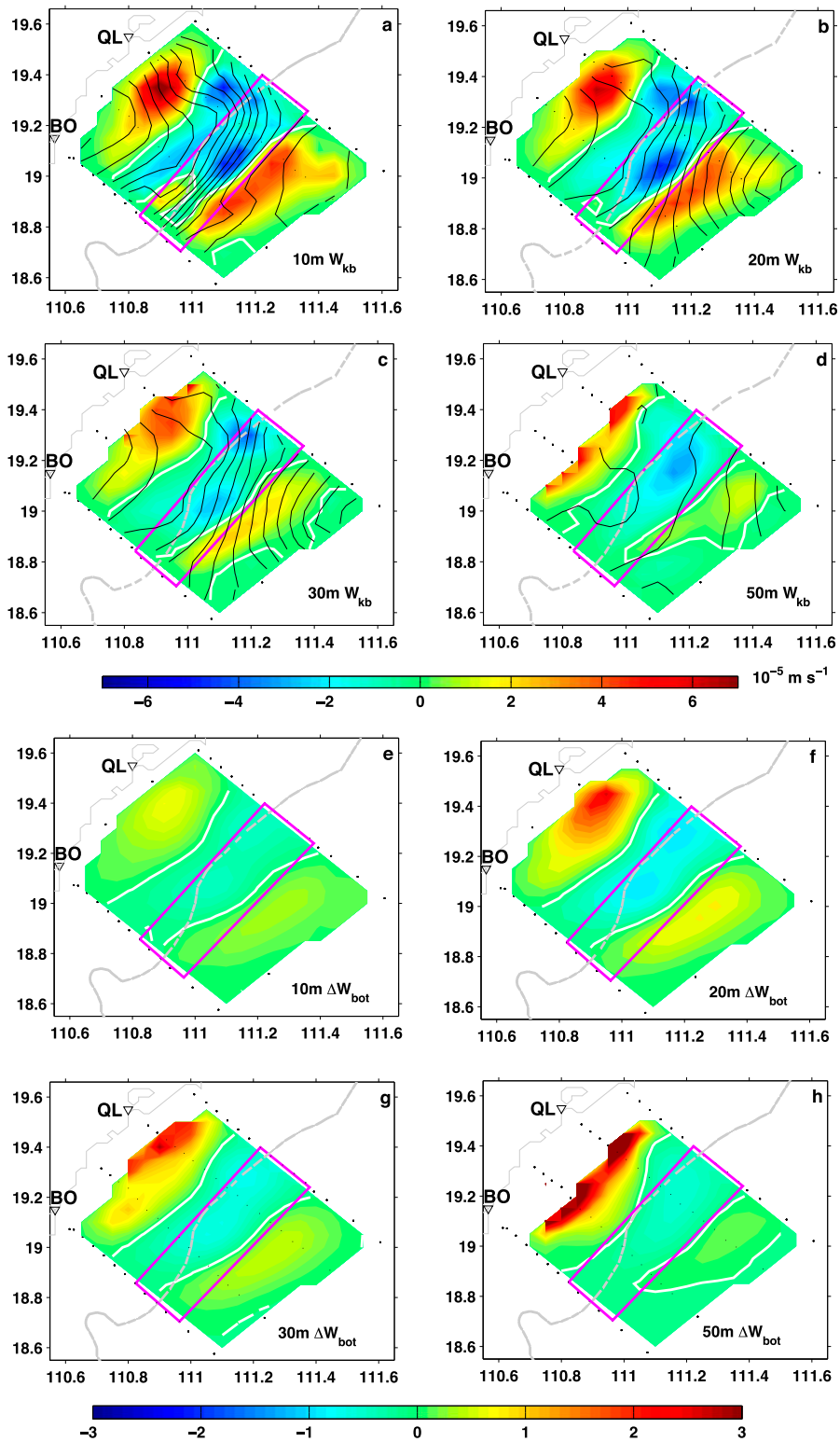
FIG. 18. As in Fig. 12, but for (a)–(d) vertical velocity W_{kb} (kinetic bottom boundary condition) and (e)–(h) the difference ΔW_{kb} between W_{kb} and W (zero bottom boundary condition).

Zhang et al. 2014; Sun et al. 2015). Our study area is about 500 km west of the ground track of the last tropical storm Doksuri, which passed over the northern SCS from 26 to 30 June 2012. Our cruise observations were carried out during a period from 13 to 18 July 2012, which was two weeks after the typhoon passage. As shown in Fig. 2, the southerly winds were steady during the whole observation period. The currents of NIOs in the study area should be quite small. The 2D spatial smoothing could also further filter out their influence. Thus, we believe that the NIO contamination to the velocity is negligible.

7. Conclusions

This study deals with the calculation of vertical circulation in the upwelling region and frontal zone east of the Hainan Island, China, using the generalized omega equation and the CTD, ADCP, and TurboMAP observations in July 2012. The effects of the kinematic deformation, the ageostrophic advection, and the vertical mixing forcing, which is derived directly from microstructure observations for the first time, on the vertical circulation are diagnosed. The major findings are summarized as follows:

1) In summer southwesterly wind season, dense water upwells near the coast east of the Hainan Island, China, where the temperature and the salinity near the surface are 5°C lower and 1 psu higher than that in the ocean area deeper than 100 m. The horizontal velocities are northeastward along the coast in the surface layer and turns anticlockwise with the depth to shoreward near the bottom, supporting the cold, salty deep waters to upwell in the coastal water.

2) A strong, frontal zone with the density gradient of $O(10^{-4})$ kg m^{-4} appears along the 100-m isobath in the subsurface layer. In the frontal zone, the kinetic energy dissipation rate ε and the vertical eddy diffusivity K_v on the shoreward (dense water) side are one order of magnitude smaller than that on the seaward (light water) side. Alongshore bands of high and low mixing rate alternatingly appear in the cross-shelf direction.

3) The diagnosis dynamic terms of kinematic deformation S_{DEF}, ageostrophic advection S_{ADV}, and vertical mixing effect S_{MIX} all show banded structure with a horizontal spatial scale of about 20 km distributed in the cross-shelf direction. Term S_{DEF} is dominated by the ageostrophic component S_{DEFa} and dominant in the frontal zone. The term S_{ADV} is the largest one in the shallow coastal waters and at the bottom layer. The mixing effect S_{MIX} on the vertical circulation should be considered in the upper ocean, especially at depths with relatively large vertical eddy diffusivity and eddy diffusivity gradient in the frontal zone but is negligible in deep layers below thermocline.

4) Consistently with the banded structure of the dynamic terms, alternating alongshore upwelling and downwelling bands appear from the coast to the deep water in the observation area. The maximum downwelling velocity reaches -5×10^{-5} m s^{-1} in the frontal zone near the 100-m isobath, while upwelling on two sides of the frontal zone has comparable maximum vertical velocities of $5 \sim 7 \times 10^{-5}$ m s^{-1}. The stronger upwelling band near the coast can be attributed to the nonlinear Ekman suctions due to the interaction of wind and vorticity gradient.

REFERENCES

Allen, J. T., and D. A. Smeed, 1996: Potential vorticity and mesoscale vertical velocity at the Iceland–Færoes front. *J. Phys. Oceanogr.*, **26**, 2611–2634, doi:10.1175/1520-0485(1996)026<2611:PVAVVA>2.0.CO;2.

——, and Coauthors, 2005: Diatom carbon export enhanced by silicate upwelling in the northeast Atlantic. *Nature*, **437**, 728–732, doi:10.1038/nature03948.

Barth, J. A., and Coauthors, 2007: Delayed upwelling alters nearshore coastal ocean ecosystems in the northern California Current. *Nature*, **104**, 3719–3724, doi:10.1073/pnas.0700462104.

Capet, X., J. C. McWilliams, M. J. Molemaker, and A. F. Shchepetkin, 2008: Mesoscale to submesoscale transition in the California current system. Part II: Frontal processes. *J. Phys. Oceanogr.*, **38**, 44–64, doi:10.1175/2007JPO3672.1.

Deng, S., H. L. Zhong, M. W. Wang, and F. J. Yu, 1995: On relation between upwelling off Qionghai and fishery (in Chinese). *J. Oceanogr. Taiwan*, **14**, 51–56.

Ferrari, R., 2011: A frontal challenge for climate models. *Science*, **332**, 316–317, doi:10.1126/science.1203632.

Giordani, H., L. Prieur, and G. Caniaux, 2006: Advanced insights into sources of vertical velocity in the ocean. *Ocean Dyn.*, **56**, 513–524, doi:10.1007/s10236-005-0050-1.

Guo, F., and M. C. Shi, 1998: Two-dimensional diagnosis model to calculate upwelling on offshore of the east coast of Hainan Island (in Chinese). *Acta Oceanol. Sin.*, **20**, 109–116.

Han, Y. W., M. B. Wang, and K. M. Ma, 1990: On the lowest surface temperature area of China Sea in summer—The upwelling along the east coast of Hainan Island (in Chinese). *Oceanol. Limnol. Sin.*, **21**, 267–275.

He, Q., Z. X. Wei, and Y. G. Wang, 2012: Study on the sea currents in the northern shelf and slope of the South China Sea based on the observation (in Chinese). *Acta Oceanol. Sin.*, **34**, 17–28.

Hoskins, B. J., I. Draghici, and H. C. Davies, 1978: A new look at the **ω**-equation. *Quart. J. Roy. Meteor. Soc.*, **104**, 31–38, doi:10.1002/qj.49710443903.

Hu, J. Y., J. P. Gan, Z. Y. Sun, J. Zhu, and M. H. Dai, 2011: Observed three-dimensional structure of a cold eddy in the southwestern South China Sea. *J. Geophys. Res.*, **116**, C05016, doi:10.1029/2010JC006810.

Jing, Z. Y., Y. Q. Qi, Y. Du, S. W. Zhang, and L. L. Xie, 2015: Summer upwelling and thermal fronts in the northwestern South China Sea: Observational analysis of two mesoscale mapping surveys. *J. Geophys. Res.*, **120**, 1993–2006, doi:10.1002/2014JC010601.

McWilliams, J. C., 2016: Submesoscale currents in the ocean. *Proc. Roy. Soc. London*, **A472**, 20160117, doi:10.1098/rspa.2016.0117.

Nagai, T., A. Tandon, and D. L. Rudnick, 2006: Two-dimensional ageostrophic secondary circulation at ocean fronts due to vertical mixing and large-scale deformation. *J. Geophys. Res.*, **111**, C09038, doi:10.1029/2005JC002964.

——, ——, N. Gruber, and J. C. McWilliams, 2008: Biological and physical impacts of ageostrophic frontal circulations driven by confluent flow and vertical mixing. *Dyn. Atmos. Oceans*, **45**, 229–251, doi:10.1016/j.dynatmoce.2007.12.001.

——, ——, H. Yamazaki, M. J. Doubell, and S. Gallager, 2012: Direct observations of microscale turbulence and thermohaline structure in the Kuroshio Front. *J. Geophys. Res.*, **117**, C08013, doi:10.1029/2011JC007228.

Naveira Garabato, A. C., J. T. Allen, H. Leach, V. H. Strass, and R. T. Pollard, 2001: Mesoscale subduction at the Antarctic Polar Front driven by baroclinic instability. *J. Phys. Oceanogr.*, **31**, 2087–2107, doi:10.1175/1520-0485(2001)031<2087:MSATAP>2.0.CO;2.

Osborn, T. R., 1980: Estimates of the local-rate of vertical diffusion from dissipation measurements. *J. Phys. Oceanogr.*, **10**, 83–89, doi:10.1175/1520-0485(1980)010<0083:EOTLRO>2.0.CO;2.

Pallàs-Sanz, E., and A. Viúdez, 2005: Diagnosing mesoscale vertical motion from horizontal velocity and density data. *J. Phys. Oceanogr.*, **35**, 1744–1762, doi:10.1175/JPO2784.1.

——, T. M. Johnston, and D. L. Rudnick, 2010a: Frontal dynamics in a California Current System shallow front: 1. Frontal processes and tracer structure. *J. Geophys. Res.*, **115**, C12067, doi:10.1029/2009JC006032.

——, ——, and ——, 2010b: Frontal dynamics in a California Current System shallow front: 2. Mesoscale vertical velocity. *J. Geophys. Res.*, **115**, C12068, doi:10.1029/2010JC006474.

Pollard, R. T., and L. A. Regier, 1992: Vorticity and vertical circulation at an ocean front. *J. Phys. Oceanogr.*, **22**, 609–625, doi:10.1175/1520-0485(1992)022<0609:VAVCAA>2.0.CO;2.

Rudnick, D. L., 1996: Intensive surveys of the Azores front: 2. Inferring the geostrophic and vertical velocity fields. *J. Geophys. Res.*, **101**, 16 291–16 303, doi:10.1029/96JC01144.

Shearman, R. K., J. A. Barth, and P. M. Kosro, 1999: Diagnosis of the three-dimensional circulation associated with mesoscale motion in the California Current. *J. Phys. Oceanogr.*, **29**, 651–670, doi:10.1175/1520-0485(1999)029<0651:DOTTDC>2.0.CO;2.

Stern, M. E., 1965: Interaction of a uniform wind stress with a geostrophic vortex. *Deep-Sea Res. Oceanogr. Abstr.*, **12**, 355–367, doi:10.1016/0011-7471(65)90007-0.

Su, J., and T. Pohlmann, 2009: Wind and topography influence on an upwelling system at the eastern Hainan coast. *J. Geophys. Res.*, **114**, C06017, doi:10.1029/2008JC005018.

Sun, Z. Y., J. Y. Hu, Q. A. Zheng, and J. P. Gan, 2015: Comparison of typhoon-induced near-inertial oscillations in shear flow in the northern South China Sea. *Acta Oceanol. Sin.*, **34**, 38–45, doi:10.1007/s13131-015-0746-0.

Thomas, L. N., and C. M. Lee, 2005: Intensification of ocean fronts by down-front wind. *J. Phys. Oceanogr.*, **35**, 1086–1102, doi:10.1175/JPO2737.1.

——, ——, and Y. Yoshikawa, 2010: The subpolar front of the Japan/East Sea. Part II: Inverse method for determining the frontal vertical circulation. *J. Phys. Oceanogr.*, **40**, 3–25, doi:10.1175/2009JPO4018.1.

Viúdez, A., J. Tintoré, and R. L. Haney, 1996: About the nature of the generalized omega equation. *J. Atmos. Sci.*, **53**, 787–795, doi:10.1175/1520-0469(1996)053<0787:ATNOTG>2.0.CO;2.

Wu, B. Y., 1990: A study on the circulation in shelf waters west to Zhujiang River mouth. II. Upwelling (in Chinese). *J. Oceanogr. Taiwan*, **9**, 331–337.

Xie, L. L., S. W. Zhang, and H. Zhao, 2012: Overview of studies on Qiongdong upwelling (in Chinese). *J. Trop. Oceanogr.*, **31**, 35–41.

Xu, Z. H., B. S. Yin, and Y. J. Hou, 2011: Multimodal structure of the internal tides on the continental shelf of the northwestern South China Sea. *Estuarine Coastal Shelf Sci.*, **95**, 178–185, doi:10.1016/j.ecss.2011.08.026.

Zhang, S. W., L. L. Xie, R. X. Cao, and H. Zhao, 2012: Observation of upper-ocean mixing in the region west of the Luzon Strait in Spring. *J. Coastal Res.*, **284**, 1208–1213, doi:10.2112/JCOASTRES-D-11-00145.1.

——, ——, H. Zhao, Y. J. Hou, Y. Q. Qi, and X. F. Yi, 2014: Tropical storm-induced turbulent mixing and chlorophyll-a enhancement in the continental shelf southeast of Hainan Island. *J. Mar. Syst.*, **129**, 405–414, doi:10.1016/j.jmarsys.2013.09.002.

Zheng, Q. A., R. J. Lai, N. E. Huang, J. Y. Pan, and W. T. Liu, 2006: Observation of ocean current response to 1998 Hurricane Georges at Gulf of Mexico. *Acta Oceanol. Sin.*, **25**, 1–14.